UNIVERSITÀ DEGLI STUDI DI PADOVA

Dipartimento di Fisica e Astronomia "Galileo Galilei"

Master Degree in Physics

Final Dissertation

Measuring the elemental composition of asteroids with a Compton telescope

Thesis supervisor

Prof. Riccardo Rando

Candidate

Sara Andreetta

Academic Year 2019/2020

Contents

List of Figures

List of Tables

Chapter 1

Introduction

The content of this work is the study of the material composition of an asteroid, using gamma-ray spectroscopy.

Gamma-ray spectroscopy among the other available spectroscopic techniques is the only method which let us study the surface to a depth of several cm, making it possible to study the composition of the medium below e.g. a layer of dust. This technique is based on the analysis of gamma rays coming from the surface of asteroid: these signals are produced mainly by the interaction of cosmic rays with the asteroid itself.

In the past several missions studied Solar System bodies (asteroids and planets) with remote sensing [1]: NEAR in particular studied the asteroid Eros with a simple gamma-ray detector and for this reason it became a baseline for our work.

We consider three different detector designs: the first one is a Compton camera with a calorimeter and a Si tracker, the second one is a Compton crystal calorimeter and the last is a remake of the NEAR instrument.

The work is based on simulations of the signals that the detectors could reveal, taking into account all the main background components, for example the diffuse gamma-ray backgrounds and the material activation in the detector itself.

Chapter 2

Scientific framework

In this chapter we will provide a brief introduction to a few minerals of interest and a short recap on the methods available to study material composition from remote.

2.1 Characterisation of minerals

The are several types of minerals present on Earth. We report here the main 8 types, based on their chemical composition.

- Silicates: they are minerals made by compounds of silicon and oxygen atoms. They represent about 90% of minerals of Earth's crust. They are subdivided in seven types; some examples of silicates minerals are olivine and quartz.

- Sulfides: they are minerals based on the sulfur ion S_2^-, for example pyrite and galena.

- Oxides: they are compound based on the oxygen anion O^{2-}, for example hematite and magnetite.

- Halides: they are minerals in which the anion is a halogen element, for example the compound NaCl.

- Sulfates: they are minerals based on the sulfate ion $(SO_4)^{2-}$, for example anhydrite.

- Phosphates: they are minerals based on the phosphate ion $(PO_4)^{3-}$, for example fluorapatite.

Moreover additional elements are present in the Earth's crust, e.g. gold. In figure 2.1 the composition of the Earth's crust, of Moon's surface and meteorites are shown.

Notably, for long the analysis of meteorites originating in the fragmentation of asteroids has been the only way to study the compositions of the latter.

A more detailed classification of minerals is presented in [2].

Classes of minerals	Earth's crust	Moon	Meteorites
Simple materials, intermetallides	82	7	13
Sulfides, selenides, tellurides	245	9	21
Sulfosalts	256	–	–
Arsenides, antimonides, bismutides	62	–	–
Oxides	212	20	26
Hydroxides	180	1	2
Silicates	883	37	73
Carbonates	165	1	7
Sulfates	293	–	3
Phosphates	352	5	13
Arsenates	198	–	–
Vanadates	64	–	–
Molibdates, wolframates	25	–	2
Chromates	6	–	–
Borates	128	–	–
Nitrates	15	–	–
Tellurites, selenites, tellurates, selenates	57	–	–
Iodates	8	–	–
Fluorides	42	–	–
Chlorides, oxychlorides	82	1	2
Bromides, iodides	6	–	–
Carbides, phosphides, nitrides	17	3	11
Silicides	5	–	1
Organic compounds	30	1	1
Total number of mineral species	3413	85	175

Figure 2.1: Numbers of minerals of different chemical classes in the Earth's crust, Moon and meteorites [2].

2.1.1   Characterisation of meteorites

Meteorites, which are constituted of different minerals, are divided into 3 main classes.

- Stony meteorites: they are the largest group (about the 95% of total meteorites) and they once formed part of the outer crust of a planet or asteroid.

  Chondrite meteorites contain grain-like inclusions name chondrules, indicating no further reprocessing of the original material. Achondrites, on the other hand, are more similar to basalts and indicate reprocessing and melting of the original material.

  Chondrites are classified further by the total amount of iron into H (15–20% Ni/Fe), L (7–11 % Ni/Fe) and LL(3–5% Ni/Fe). In figure 2.2 the difference between the

Minerals	H-chondrites	L-chondrites
Olivine	36.2	47.0
Hypersthene	24.5	22.7
Diopside	4.0	4.6
Plagioclase	10.0	10.7
Apatite	0.6	0.6
Chromite	0.6	0.6
Ilmenite	0.2	0.2
Troilite	5.3	6.1
Fe–Ni metal (kamacite + taenite)	18.6	7.5

Figure 2.2: Composition of chondrites with Low-iron and High-iron abundances.

mineral composition of High-Iron chondrites and Low-Iron Chondrites is shown [3].

- Iron meteorites are formed by about 90% of Fe/Ni/Co; iron meteorites are believed to have formed within the Asteroid Belt and represent about 3% of meteorites.

- Stony-Iron meteorites: they are less than 2% of total known meteorites. They have almost equal quantity of iron and stone.

Chondrites are the most common type of meteorites and we will consider for this work an asteroid with the same composition.

For more details about the asteroid used in this work see section 5.2.

2.2 Spectroscopic techniques

2.2.1 IR spectroscopy

IR spectroscopy is based on infrared radiation with matter: light impinges on the target and a modified spectrum is observed either in transmission on reflection. The latter approach makes remote sensing possible.

The energy interval in which it is useful is from $\sim$5 meV to $\sim$1.5 eV ; in this range the electromagnetic spectrum is divided in three different regions:

- Far-Infrared: it is the region with the lowest energy (25–303.3 µm) and it is used to study vibrations of molecules containing heavy atoms, molecular skeleton vibrations and torsions and also crystal lattice vibrations;

- Mid-Infrared: it is the region (2.5–25 µm) useful to study the fundamental vibrations and associated rotational-vibrational structure of matter; chemical bonds have being studied with this method;

- Near-Infrared: it is the region with the highest energy (0.78–2.5 µm) and this radiation can excite overtone and harmonic frequencies.

Several type of sensors are used to detect IR photons, operated either as photon counters or bolometers, employing a variety of physical processes. A commonly used material is HgCdTe, a compound with a tunable bandgap that can be coupled to conventional CCD sensors. Filters or refractive optics can be used to direct only one narrow spectral band.

A common requirement of IR detectors is cooling, operating temperature range from room temperature to 77 K depending on the wavelength range of interest.

Using IR scattering targets can be investigated to a depth of $\sim$1 mm.

IR spectra show a large variety of features; huge database are available with reference IR spectra for various minerals which are useful for the analysis.

This technique was applied e.g. to study the presence of water on the Moon's surface [4].

2.2.2   X-ray spectroscopy

The X-ray spectroscopy is based on the interaction of X-ray radiation with matter: when an electron from the inner shell of an atom is excited by the energy of a photon (coming for example from the Sun), it moves to a higher energy level. The energy gained by the excitation is then emitted as a photon which has a wavelength that is characteristic for the element.

Analysing the X-ray emission it is possible to know the elemental composition of the material studied. The energy range covers the interval 0.1–100 keV.

Instruments that work with this method are crystal spectrometers (they work in almost the same way of IR spectrometer) and proportional counters, in which the electrical response is proportional to the deposited energy. A key parameter for X-ray sensors is the energy resolution, since the elements emit lines with varying intensities that must be separated.

This technique had been used e.g. in the Apollo missions to measure the abundance of Al on the Moon's surface [5].

2.2.3   Gamma-Ray spectroscopy

Gamma rays are produced by the decay of relic radioactive isotopes and of radioisotopes generated by the irradiation of cosmic rays.

Gamma-ray detectors can employ any of the interaction mechanisms for gamma-ray photons in matter: photoelectric effect, Compton scattering and pair production, depending on energy and material. In gaseous and semiconductor mediums ionization of secondaries is directly converted into an electric signal, while in scintillating materials ionization causes an optical light pulse.

Gamma-ray spectroscopy is possible when the energy resolution of the system is sufficient and it is of particular interest since it allows to study materials to a depth of few cm's, therefore it is less sensitive to e.g. a layer of dust on the surface of the target.

This method had been used e.g. in Apollo missions to study the elemental composition of the Moon's surface [6].

Chapter 3

Historical framework

3.1 Study of Lunar composition

Before 1960, all the knowledges about the Moon came from studies performed with Earth-based telescopic experiments; then, between 1960 and 1970, many programs initiated by the United States and the Soviet Union gave a new point of view.

In particular, the first chemical analysis in-situ were made during the Surveyor program, while the first orbital analysis were made by several experiments before 1965.

The first phase of remote sensing was a trial phase, in which Ranger 3, Ranger 5, Luna 10 and Luna 12 started to study the material composition of the Moon.

- Ranger 3 and Ranger 5 were two American mission whose aim was reaching the Moon. They had a detector for gamma-ray spectroscopy, which was constituted by a cylindric crystal of CsI of about 7 cm × 7 cm with plastic scintillator around as anti-coincidence; its resolution was about 12% at 662 keV [7]. The mode was a fly-by at an altitude of ∼700 km.

  This experiment measured space background gamma rays (the spectrum is shown in figure 3.1), while the time mission was too short to provide fine scale geochemical mapping of the Moon [8] . They excluded that the origin of cosmic gamma rays could have been synchrotron. The absence of a line at 511 keV excluded the possibility that those gamma rays could have been originated in nuclear interactions of high-energy particles [9].

- Kosmos 60 in 1965 collected and analysed the first Russian data about gamma rays in space. Russian Luna-10 and Luna-12 had a gamma-ray spectrometer formed by a NaI crystal. There was 32 channel energy resolution over the energy range 0.3–3 MeV. The mode was a fly-by at an altitude of of ∼350 km.

  It was shown that the 90% of the intensity of gamma-ray radiation is due to cosmic ray interactions, while less than 10% is due to the decay of radioactive nuclides (e.g. U, Th and K) contained in lunar rocks. These studies demonstrated that the total level of gamma-ray radiation intensity from the lunar surface was almost
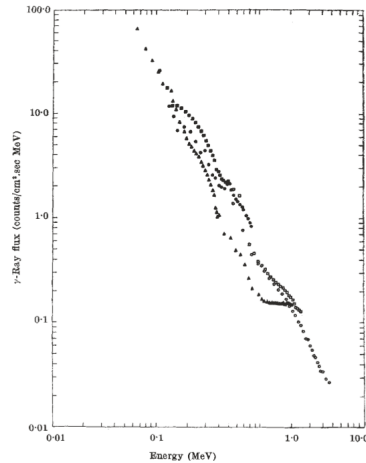
Figure 3.1: Cislunar spectrum obtained by Ranger 3 and Ranger 5.

2 times higher than the level of terrestrial rocks as granite; their conclusions had been confirmed also by the results of Surveyor program.

The gamma spectrum showed an exponential decrease up to ∼1.5 MeV, while being roughly flat above that energy (see figure 3.2) [10].
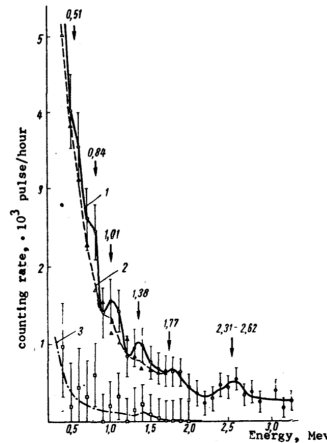
Figure 3.2: Gamma spectrum with indication of the lunar composition by Luna-10

In July 1969 Apollo astronauts brought back samples of lunar materials (basalts) allowing for direct analysis in the laboratory. In order to obtain a more complete compositional map of the Moon, many remote sensing experiment were proposed.

- Apollo 15 and Apollo 16 also had a gamma-ray spectrometer on board: the instrument was constituted by a cylindrical crystal of NaI 7 cm × 7 cm, which had

a thin scintillating plastic crystal isolated from the NaI cylinder as cover. The energy resolution of the NaI detector at 0.661 MeV was 8.5% (Apollo 15) and 7.5% (Apollo 16). The orbits were nearly circular and at an altitude of about 120 km.

The collected spectra showed different characteristic lines superimposed on a continuum.

- The American spacecraft Lunar Prospector had a gamma-ray detector, which was formed by a bismuth germanate (BGO) scintillator encased by a plastic anticoincidence shield (ACS). The gamma-ray energy extended between 0.3 MeV and 9.0 MeV, while the energy resolution at 662 keV was about 8% at Full Width at Half Maximum (FWHM).

  Detailed maps showing presence of Th, K and Fe were obtained [11].

- The more recent Japanese spacecraft Selene (Kaguya) had a High-Purity germanium HPGe crystal as the main detector and a BGO scintillator for anticoincidence. It was the first use of a Ge detector for lunar exploration [12]. The most important feature for the HPGe detector was its excellent high energy resolution (e.g. of 3.0 keV at 1.332 MeV), which permitted the identification of individual gamma-ray lines in a complex-shaped peak. The orbit was circular polar at 100 km.

  The detector was able to identify many subsurface elements such as O, Mg, Al, Si, K, Ca, Ti, Fe, U, and Th, providing global composition maps of the Moon [13].

- The Chinese Chang'e-1 was launched in October 2007. One of the payloads was a gamma-ray spectrometer, whose objectives were mapping abundances of O, Si, Fe, Ti, U, Th, K, Mg, Al, and Ca, to depths of about 20 cm. The detector was formed by a CsI cylinder of dimensions 11.8 cm × 7.8 cm; its energy resolution was 8.2% FWHM at an energy of 662 keV [14] – [15]. The orbit was polar and at an altitude of 200 km.

3.2   Study of planetary composition

- The first mission that studied the composition of Venus was the Russian Venera 8, launched in 1972. The lander sent about 50 minutes of data after having reached the surface of the planet. The detector was a crystal of CsI with an energy resolution of ∼10% at 662 keV.

  Moreover data from the gamma-ray spectrometer determined the naturally occurring radioactive elemental abundance in the soil: preliminary data suggested that the surface material contained 4% K, 0.002% U and 0.00065% Th [16].

- In 1974 the Russian spacecraft Mars 5 was sent to study the planet Mars with a gamma-ray spectrometer made by a HpGe crystal, whose energy resolution was ∼0.3% at 1.332 MeV. The average altitude above the surface planet, at which measurements were taken, was 2000 km.
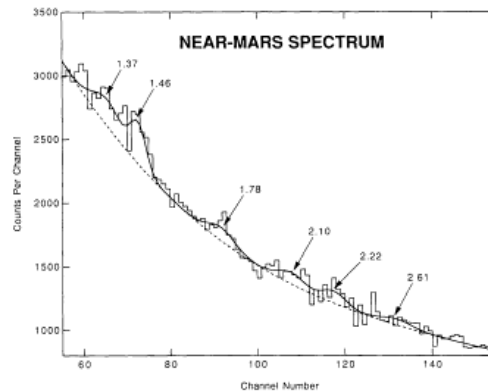
Figure 3.3: Spectrum of gamma radiation measured by Phobos2.

The surface concentrations of natural radioactive nuclides in the martian surface were similar to igneous rocks present in the terrestrial crust [17].

In 1988 a Russian spacecraft, Phobos 2, was launched to reach Mars. The aim of the experiment was to determine the content of the basic rock-forming elements (O, Mg, Al, Si, Ca, and Fe) and the abundance of natural radioactive nuclides (U, Th, and K). The orbit was elliptical equatorial, with periapsis ∼800 km and apoapsis ∼9000 km.

The gamma-ray spectrometer was used also to collect data from cosmic gamma-ray burst and high-energy radiation of solar flares.

The detector was constituted by a scintillation crystal of CsI with an energy resolution at 0.662 MeV of about 12 % and it recorded gamma-ray in an energy range between 0.1 MeV and 10 MeV. It was mounted on the far edge of the solar panel, in order to reduce the background of gamma-ray radiation caused by the induced radioactivity of the spacecraft.

In figure 3.3 the original data taken from the instrument are shown: the fitted background (the dashed line) and the fitted peaks, with their energy value in MeV, are plotted [18].

The American Mars Observer, launched in 1992, differently from the predecessors, had a gamma-ray detector that was constituted by a large single crystal of ultrahigh-purity germanium HPGe, with dimensions 5.5 cm × 5.5 cm [19].

Unfortunately the mission failed and not useful informations have been found out.

However, the same gamma-ray spectrometer was mounted on the American 2001 Mars Odyssey, launched in April 2001. The HPGe detector had collected data from gamma-ray of energies between 0.1 MeV and 10 MeV, whit energy resolution ∼0.3%; it was possible to determine from the orbit (circular polar at altitude of 400 km) the concentration of elements presented in the planet.

Several elemental concentration maps have been developed and they have been used to constrain hypotheses concerning the processes that affected the planet since its formation [20].

- The NASA spacecraft Messenger was launched in 2004 in order to reach Mercury. There was a gamma-ray and neutron spectrometer that have yielded maps of the elemental composition of planet surface.

  The HPGe detector of gamma rays had an energy resolution of 0.3% at 1332 keV and it recorded events in the energetic range 0.1–10 MeV. The orbit was elliptical polar at an average altitude of ∼400 km [21].

3.3 Study of asteroids

We report the main missions that had already investigated on asteroids through remote sensing.

- Galileo, launched in 1989, had the aim of study asteroids Gaspra and Ida, using IR spectroscopy;

- NEAR Shoemaker, launched in 1996, had the aim of study asteroid Eros, using IR, X-ray and gamma-ray spectroscopy (see chapter 4 for more details);

- Cassini, launched in 1997, had the aim of study asteroid Masursky, using IR spectroscopy;

- Deep Space 1, launched in 1998, had the aim of study asteroid Braille, using IR spectroscopy;

- Stardust, launched in 1999, had the aim of study asteroid Annefrank, using IR spectroscopy;

- Rosetta, launched in 2004, had the aim of study asteroids Steins and Lutetia, using IR spectroscopy;

- DAWN, launched in 2007, had the aim of study asteroid Vesta, using both IR and gamma-ray spectroscopy (see section 3.3.1);

- Hayabusa, launched in 2003, had the aim of study asteroid Itokawa, using both IR and X-ray spectroscopy;

- Hayabusa 2, launched in 2014, had the aim of study asteroid 1999 JU3, using IR spectroscopy;

- OSIRIS-REx, launched in 2016, had the aim of study asteroid Bennu, using both IR and X-ray spectroscopy;

3.3.1   The DAWN mission

DAWN was a NASA discovery mission that explored two of the largest main-belt asteroids, Ceres and Vesta. The aim was to determine the composition and the structure of these bodies, in order to understand what happened after the onset of condensation of the Solar nebula.

The detector for gamma-ray spectroscopy was formed by 4×4 array of coplanar grid CdZnTe semiconductor detectors that worked as the primary gamma-ray spectrometer. Each element in that array contained a 10 mm $\times$ 10 mm $\times$ 7.5 mm CdZnTe crystal and it had an energy resolution of about 3% FWHM at 662 keV. The orbit was circular with altitude of $\sim$400 km.

The spectroscopy scintillator was part of a more complex gamma ray and neutron detector (GRAND) [22].

The mission performed also an experiment to determine the magnitude of the damage effects: the detector in fact was exposed to protons with a mean energy of 153.7 MeV. It was found that reduction in resolution due to radiation damage of CdZnTe by energetic particles in the space environment could be mitigated by including a capability for annealing at elevated temperatures on Dawn [23].

With data collected by the gamma-ray spectrometer it was possible to construct an elemental map for the asteroids, distinguishing different regions with characteristic properties.

3.3.2   Study of asteroid 16 Psyche

The Psyche mission is one of the discovery orbital missions concepts that was selected by NASA. The asteroid 16 Psyche is a metal-rich type and it is similar to Fe meteorites; it will be visited in 2026 by Psyche spacecraft.

The main objectives of the experiments are:

- characterise the bulk Ni content, from which it is possible to find important informations about the thermal evolution of the core;

- analyse the composition of the silicates, that could be remnants of the original mantle of the asteroid;

- measure the light element content of the metal in order to understand light-element partitioning into cores during differentiation.

The Psyche spacecraft payload includes a Gamma-Ray and Neutron Spectrometer. The gamma-ray detector consists of a high-purity germanium HPGe surrounded by a borated plastic anti-coincidence shield (ACS). The HPGe detector has an energy resolution of 4.0 keV at 1332 keV and it measures gamma-ray emission from the asteroid; the ACS is used to remove the galactic cosmic-ray induced background in the gamma-ray spectrum via veto rejection. It reduces the background continuum of a factor 6 at 7 MeV and of a factor 2.5 at 3 MeV, at an altitude of 1.3 body radii.

Differently from the previous mission Messenger, the gamma-ray spectrometer will be located at the end of a 2-meter-long boom, in order to have a significant reduction in the spacecraft-originating backgrounds seen by the instrument.

DAWN team model cosmogenic radionuclide production using Geant4, an approach similar to this work. They report that galactic cosmic-ray induced radionuclide production and decay will not be observable from orbit by the Psyche gamma-ray spectrometer. In contrast, solar-cosmic-ray-induced radionuclide decay, produced during a solar proton event with energy above 30 MeV, may be observable during the 100-day-long low-altitude orbit at Psyche [24] – [25].

Object	Year	Mission	Country	Detector	Anti-coincidence	Location	Max energy [MeV]
Moon	1962	Ranger 3	USA	CsI(Tl)	Plastic scintillator	Boom (1.8 m)	2.0
Moon	1962	Ranger 5	USA	CsI(Tl)	Plastic scintillator	Boom (1.8 m)	2.0
Moon	1966	Luna 10	USSR	NaI(Tl)	Plastic scintillator	Integrated	3.0
Moon	1966	Luna 12	USSR	NaI(Tl)	Plastic scintillator	Integrated	3.0
Moon	1971	Apollo 15	USA	NaI(Tl)	Plastic scintillator	Boom (7.6 m)	10.0
Moon	1972	Apollo 16	USA	NaI(Tl)	Plastic scintillator	Boom (7.6 m)	10.0
Moon	1998	Lunar Prospector	USA	BGO	B-loaded plastic scintillator	Boom (2.5 m)	10.0
Moon	2007	Kaguya	JPN	HPGe	BGO, Plastic scintillator	Integrated	12.0
Moon	2007	Chang'e-1	CHN	CsI(Tl)	CsI(Tl)	Integrated	9.0
Venus	1972	Venera 8	USSR	CsI(Tl)	none	Integrated	3.0
Mars	1974	Mars 5	USSR	CsI(Tl)	none	Integrated	3.0
Mars	1988	Phobos 2	USSR	CsI(Tl)	none	Integrated	4.0
Mars	1992	Mars Observer	USA	HPGe	B-loaded plastic scintillator	Boom (6.0 m)	10.0
Mars	2001	2001 Mars Odyssey	USA	HPGe	B-loaded plastic scintillator	Boom (6.2 m)	10.0
Mercury	2004	Messenger	USA	HPGe	B-loaded plastic scintillator	Integrated	10.0
Eros	1996	NEAR	USA	NaI(Tl)	BGO	Integrated	10.0
Vesta, Ceres	2007	DAWN	USA	BGO CZT array	B-loaded plastic scintillator	Integrated	10.0

Table 3.1: Main gamma-ray sensing experiments.

Chapter 4

The Near Earth Rendezvous Mission

The Near Earth Asteroid Rendezvous (NEAR) mission was the first attempt to orbit an asteroid and it made the first scientific measurements of its surface composition, geology and physical properties. NEAR was launched in 1996 and, after some troubles, on February 2000 it entered orbit around the asteroid 433 Eros, a large asteroid near Earth. The spacecraft landed on Eros on February 2001 ending its mission.

The gamma-ray detector on board had a simple geometry based on heritage from the Apollo missions.

We decided to perform our analysis under NEAR-like conditions.

4.1 The NEAR mission

The NEAR mission spent about a year in orbit around Eros. It acquired the first comprehensive and spatially resolved data of the geomorphology, reflectance spectral properties, shape of an asteroid, X-ray and gamma-ray measurements of the elemental abundances from the asteroid's orbit and surface, ambient magnetic field near the asteroid.

NEAR orbited Eros at low altitude, about one body radius above the surface, for more than six months. The spacecraft contained six different scientific instruments as payloads: Multispectral Imager, Near-Infrared Spectrograph, X-Ray spectrometer, Gamma-Ray Spectrometer, NEAR Laser Rangefinder and Magnetometer [26]. The Gamma-Ray Spectrometer (indicated by GRS in figure 4.1) is integrated in the spacecraft and not located on a boom [27].

The gamma-ray spectrometer could measure the abundances of key elements at Eros with a maximum spatial resolution of about 2 km.

NEAR data, in particular when combined with data from the Galileo flybys of Gaspra and Ida, could greatly advanced the understanding of asteroids and their possible relationships to other small bodies of the solar system.
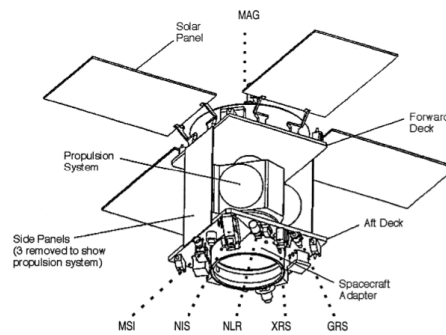
Figure 4.1: Spacecraft's structure with indication of the payloads.

NEAR asteroid target: 433 Eros

The NEAR mission had one main target: the 433 asteroid Eros.

433 Eros is the second largest Near Earth Asteroid (NEA), its mean diameter is about 20 km and so it is one order of magnitude larger than the typical known NEAs. It has density of 2.67 $g\,cm^{-3}$, its mass is $6.69 \cdot 10^{15}$ kg and it orbits the Sun with a semi-major axis of 1.46 AU and eccentricity 0.22.

During 1975, since the asteroid passed within 0.15 AU of Earth, observations from ground-based instruments allowed to determine the approximate size, shape, rotation rate and pole position of Eros.

One side of the asteroid showed an IR spectrum consistent with high pyroxene content, while the other side had a higher olivine content. The detection of variations with rotation phase in disk-averaged data suggested that substantial geologic and compositional complexity could be found at higher spatial resolution with the NEAR mission.

Gamma-Ray Spectrometer

The Gamma-Ray Spectrometer of the NEAR mission detected characteristic gamma rays emitted in the energy range between 0.3–10 MeV. The NEAR mission had a NAI(Tl) scintillator situated within a thick cup shield fabricated from a single crystal of BGO. This cup was used as an active veto and it worked to reduce the Compton and pair-production contributions to the unwanted background signal; moreover it provided a direct and passive shielding from the local gamma environment.

The NaI scintillator was a cylinder 2.54 cm × 7.62 cm and it was coupled to 3.17 cm diameter metal ceramic photomultiplier tube; outside there was a BGO scintillator cup that has outside dimensions 8.9 cm × 14 cm and it had a thickness of ∼3 cm. The total mass of the gamma-ray spectrometer was ∼6 kg.

The measured energy resolution for the NaI(Tl) was 8.7 % FWHM at an energy of 662 keV, while for the BGO was 14% FWHM [28].

Moreover it was found that the presence of the small PMT between the NaI crystal and the gamma-ray source (figure 4.2) caused an overall loss in efficiency for the NaI detector, that depended both on energy and on the angle. The light output of the two
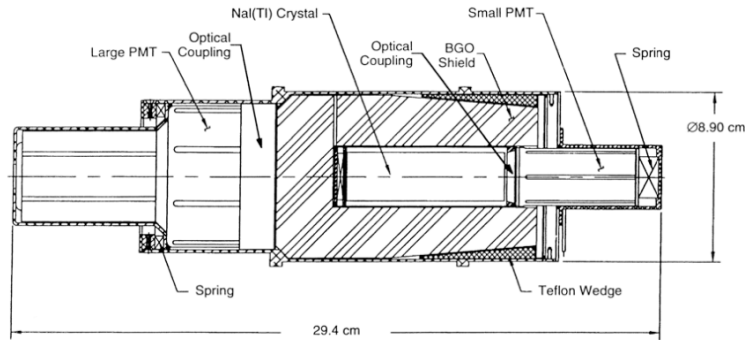
Figure 4.2: NEAR gamma-ray detector section.

detectors strongly depended on temperature: for this reason the detector assembly was thermally isolated with active control to make the gamma-ray detector working at a fixed temperature. Since the electron gain of the PMTs was sensitive to voltage variations, the PMT high voltage power supplies must be stable to a fraction of a Volt in order to not affect the gamma-ray spectrometer calibration.

The disadvantage of using a NaI scintillator instead of a HPGe detector was a worst energy resolution, but the advantage was that the NaI instrument could operate at room temperature and that it was not subjected to any serious radiation damage: this last point was really important since an operative life of many months was planned.

Calibration of the gamma-ray spectrometer

The instruments used on NEAR had been calibrated in order to know the detector response, efficiency and shield effectiveness. In the first step a lot of radioactive sources were used, such as $^{141}_{58}$Ce for low energy, $^{137}_{55}$Cs at middle energies and $^{24}_{11}$Na for higher energies. The sources were placed at known distances from the detector and along the cylinder axis; from the data collected, the efficiency and the resolution of the detector were determined as a function of the energy.

In figure 4.3 the Compton continuum and the photopeak are shown; moreover it is clear that the effect of the BGO shield was suppressing the Compton background, improving then the signal-to-noise ratio.

The figure 4.4 shows a measurements of the natural background with the anticoincidence shield on and off: the improvement in the definition of the photopeaks for the natural radioactive lines from K, U and Th when the anticoincidence shield was working is shown.

The background was mainly due to cosmic rays.

Data reduction and analysis

The output produced by the gamma-ray spectrometer must be corrected for a number of factors in order to determine the incident photon spectra from the asteroid.
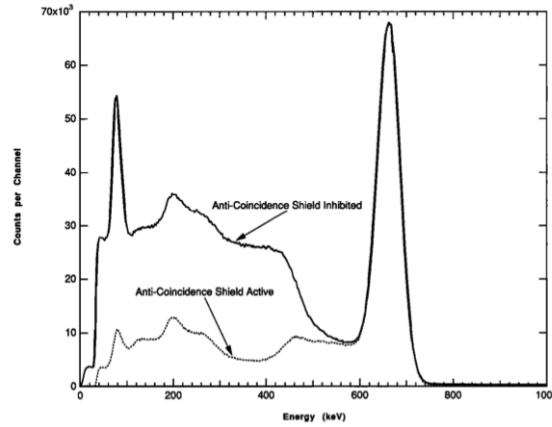
Figure 4.3: Pulse height spectrum of a $^{137}_{55}$Cs source (661 keV) measured with the NEAR gamma-ray detector. The spectra were those obtained with the NaI crystal. Spectra obtained with the anticoincidence shield both inhibited and active are shown.
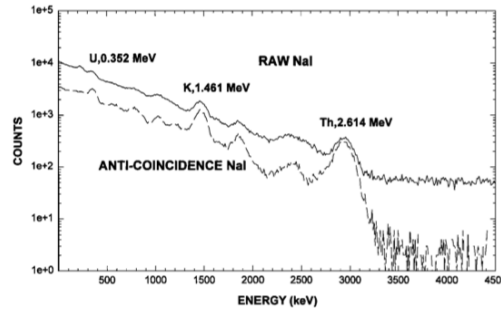
Figure 4.4: Measure of the pulse height spectrum of the material background using the NEAR NaI gamma-ray detector. Spectra with the shield both inhibited and active are shown.

Once the incident flux was determined, qualitative and quantitative informations about the composition could be inferred.

First the count spectra must be adjusted to a common energy scale, then the pulse height spectra were accumulated over the geographic region of interest (if the solar energy spectrum or the cosmic ray flux had changed, these changes were considered), then geometrical corrective factors had been applied in spectra (e.g. factors due to variation in altitude), finally the background had been subtracted.

The accumulation times for these spectra should had been long enough to be statistical meaningful in order to calibrate the energy versus pulse height scale.

Gamma-ray background had an important role: in addition to the characteristic lines emerging from the asteroid surface, there were many components due to this background, which sometimes appeared as a continuum in the spectrum and other as discrete lines.

With data collected from Apollo missions, it was possible to identify the main sources of background, which were:

- direct cosmic ray interactions in the detector;

- primary cosmic ray induced radioactivity in the detector;

- secondary neutron-induced radioactivity in the detector;

- discrete line emission produced in the local mass around the detector by cosmic ray interactions;

- electron bremsstrahlung from the local mass;

- natural and induced radioactivity in the spacecraft;

- partial absorption in the detector producing the Compton continuum and first and second escape peaks;

- multiple gamma ray scattering and bremsstrahlung produced in the lunar surface;

- cosmic diffuse gamma rays.

It was assumed that the same components of the gamma-ray background could be found also on Eros. The subtraction of gamma-ray background was quite a difficult task, since many of the background components were time dependent, so a combination of empirical and theoretical data was requested.

Once the accumulated spectra had been normalised to remove the solar activity variations, they had been summed over areas on the surface of the asteroid, weighting them according to altitude, spacecraft pointing angle and incident solar flux angle. Then each characteristic elemental line was compared to Si line as reference; after that, the intensity ratios was converted to elemental concentrations in order to create a compositional map.

A particular successful strategy consisted in selecting events tagged by a gamma escape peak ∼511 keV in the outer scintillator, indicating positron production in the core.

We could not replicate easily this feature in our analysis framework (see chapter 5), so we resorted to trying to reproduce the less effective standard approach where the outer shell was used as a veto.

4.2   Results of NEAR mission

4.2.1   Timing of the mission and limitations

Since the contact with the spacecraft was initially interrupted, the rendezvous was delayed by over 1 year; NEAR entered Eros orbit on February 2000 and it started one year long orbital mission: in that period of time, the orbit changed from circular to elliptical, at distances from the center of mass of the asteroid from 200 km to 35 km; finally NEAR completed a successful controlled descent to the surface of the asteroid .

The best quality compositional data were acquired during low altitude orbits. Three optimum periods for orbital observations were individualised. The period of useful data collection for the gamma-ray instrument however was considerably shorter than the expected 6 months period.

This was caused by the structure of NEAR, which was a fixed-body spacecraft: so observations of specific regions on the surface of Eros required pointing the entire spacecraft. Targeted pointing was limited by constraints on time for telemetry to Earth and by the fact that the solar panels had to be within ± 30° of the normal direction to the Sun.

Orbital gamma-ray observations were really restricted in terms of time. This was due to the fact that in orbits at 50 km and above, the asteroid Eros effectively filled only a small portions of the field of view, so the background overwhelmed the signal from the surface. Even in orbits located at an altitude of 35 km, the signal-to-noise ratio was very low for detecting gamma-rays from the asteroid.

4.3   Results and lessons learned

The surface composition of 433 Eros measured during quiet Sun and solar flare conditions suggested that Eros was similar in bulk composition to a range of meteorites that had experienced minimal thermal alteration since their formation at the birth of solar system. Moreover it was found that Eros was "primitive" in its chemical composition and it had not experienced global differentiation into a core, mantle and crust [29] – [30].

The gamma-ray intensity from the asteroid was very weak: they expected, for example, a signal from Fe gamma rays of 0.001 count/second on top of a background of about 0.6 count/second. So it is clear that it was really difficult for them to get a Fe signal with low uncertainty.

The NEAR team reported some important consideration useful also for future mission [31]. Such a cost constrained mission represented a hard challenge for them: these cost constraints had limited their ability to build in sufficient contingency capabilities. NEAR was moreover the first mission with fixed solar panels to orbit around a non-spherical object; further, the mission slipped a year, so the mission profile changed and, for the gamma-ray spectrometer, the time and the quality of observations changed significantly. In addition, due to the short time passed between the calibration of the instrument and the launch of the spacecraft, the NEAR team could no test and complete the calibration of the flight detector for any conditions different from those planned for the original mission profile.

The post-mission procedure analysis proved to be quite complex.

Limitations

Several considerations affect the design of similar missions. They can be summarised as follows.

- Design: the gamma-ray detector had no possibility to reconstruct direction, it only featured some non-uniform efficiency due to its elongated shape and the positioning of the PMTs. Moreover, since the instrument was located on the spacecraft and not on a boom, there was no active way of reducing the background due to material activation of the spacecraft structure.

- Materials: activation was important, e.g. the ^{209}Bi present in the detector produced the 2.61 MeV line; the decay chain of Bi contaminated measurements of the abundance of Th at the same energy.

- Energy resolution: a detector with improved energy resolution (e.g. Ge detectors) can significantly lower the continuum spectrum and increase the sensitivity to emission lines by a large factor; in figure 4.5, the relative improvement in signal-to-noise ratio in shape and width of the lines relative to the background is shown.
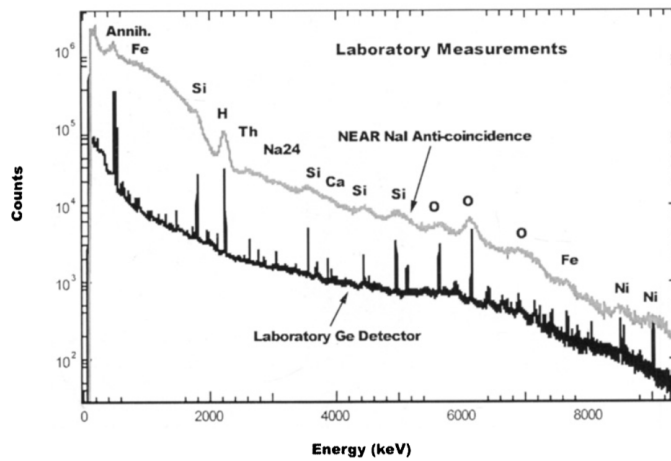
Figure 4.5: Comparison of the NEAR gamma-ray pulse height spectrum with a Ge pulse height spectrum, using a soil sample and a 14 MeV generator excitation source to simulate space environment.

Chapter 5

Analysis Set Up

In this chapter we describe the target of our study and the approach we adopted, and we give a description of the tools we used.

5.1 Plan of the activities

We want to simulate the observation of a near Earth asteroid, evaluating the issues involved and comparing the performance of three different detector designs (described in chapter 6).

The target is designed taking Eros as a general guide (see section 5.2), and the observation is simulated assuming the central phase of NEAR observations ($\sim$10 km altitude, 6 month duration).

For the simulation of the detector we employ a software framework called MEGAlib, simulating the interactions of the gamma rays with the detectors, the readout and event analysis (see section 5.3.2). For the cosmic gamma-ray spectra we use simple spectral and spatial models as inputs to MEGAlib. Activation of the detector and spacecraft can also be included.

For the simulation of the gamma rays from the asteroid such an approach is extremely inefficient, so we simulate separately the irradiation and activation of the asteroid surface using Geant4 (see section 5.3.1).

5.2 The asteroid

For the target asteroid we will consider a LL chondrite. In [32] many meteorites are analysed and material abundances in asteroids are given ranked for the percentile abundance of rare elements. One of our purposes is to evaluate if the presence of rare elements of the Pt family can be inferred from the observations to identify candidates for exploitation. As reported in table 5.1, LL-Chondrite are meteorites that contain less precious metal respect to those richer inFe. Iron meteorites can have even more, but the extraction is expected to be much more difficult [32].

Metal	Metal Abundance in H-chondrites [ppm]	Metal Abundance in LL-chondrites [ppm]
Ru	5.8	17.8
Rh	1.1	3.3
Pd	4.5	14.0
Os	3.9	12.1
Ir	3.9	12.0
Pt	8.0	24.7
Au	1.1	3.5
Sum	28.3	87.4

Table 5.1: Abundances of elements in the Pt family in chondrites, from [32].

Our asteroid has the composition of the LL-Chondrites, which represent large part of the asteroids near the Earth. In particular the abundances of precious metals have been taken by [32]; the other abundances were set according to [33] – [35].

For our simulation with Geant4, we created an asteroid made by a spherical structure of radius 8 km. For what concerns the materials of the asteroid analysed, we report in table 5.2 the elemental composition, expressed in fraction, used in the simulations work. The description of the asteroid was given in a GDML file (Geometry Description Markup Language), where materials, solids and structures have been specified.

5.3   Software

5.3.1   Geant4

Geant4 is a toolkit for simulating the passage and interaction of particles through matter. It was developed in response to several demands for accurate and comprehensive simulations of the particle detectors used in physics.

In implementing the software components, all aspects of the simulation process have been included: the geometry of the system, the materials involved, the fundamental physics of interests, the generation of primary particle events, the physics processes governing particle interactions, the response of sensitive detector components and the generation of event data.

This software is based on an abundant set of physics models to handle the interactions of particles with matter across a very wide energy range; moreover it is continually refined, expanded and developed.

Geant4 was developed by a huge international collaboration, with many contributors that have a lot of experience in the field of Monte Carlo simulation of physics detectors and physical processes [36].

We base our Geant4 simulations on an activation tool based on top of the provided examples ("RadioactiveDecay"), scoring alla the gamma rays leaving the target's surface and all the radioisotopes generated in the volume.

Material fraction	Our Asteroid
SiO_2	$4.16 \cdot 10^{-1}$
TiO_2	$1.30 \cdot 10^{-3}$
Al_2O_3	$2.25 \cdot 10^{-2}$
Cr_2O_3	$5.40 \cdot 10^{-3}$
FeO	$1.74 \cdot 10^{-2}$
MnO	$3.50 \cdot 10^{-3}$
MgO	$2.52 \cdot 10^{-1}$
CaO	$1.92 \cdot 10^{-2}$
Na_2O_3	$9.50 \cdot 10^{-3}$
K_2O_3	$1.00 \cdot 10^{-3}$
P_2O_5	$2.20 \cdot 10^{-3}$
FeS	$5.79 \cdot 10^{-2}$
Fe	$2.44 \cdot 10^{-2}$
Ni	$1.07 \cdot 10^{-2}$
Co	$5.00 \cdot 10^{-4}$
Ru	$1.78 \cdot 10^{-5}$
Rh	$3.30 \cdot 10^{-6}$
Pd	$1.40 \cdot 10^{-5}$
Os	$1.21 \cdot 10^{-5}$
Ir	$1.20 \cdot 10^{-5}$
Pt	$2.47 \cdot 10^{-5}$
Au	$3.50 \cdot 10^{-6}$
Density $[\mathrm{g\,cm^{-3}}]$	3.40

Table 5.2: Material composition of the asteroid used.

Primary particles are generated from the provided user spectrum and geometry, and with starting time sampled randomly in the specified time interval. The geometry of the target (volume and composition) is provided as a GDML file.

For the modelling of hadronic interactions we use the "qgsp-bic-hp" libraries, for compatibility with the activation calculation in MEGAlib. From a preliminary investigation of the alternatives this is the principal source of systematic uncertainties in our work.

In this work, in the configuration file the primary source is defined as a G4GeneralParticleSource (GPS): it allows the description of the spectral, spatial and angular distribution of the primary source particles. With the GPS it is possible to define:

- spatial sampling: on simple surfaces such as discs, spheres and boxes;

- angular distribution: for example unidirectional, isotropic and arbitrary;

- spectrum: linear, exponential, power-law and many others.

Figure 5.1 is an example of the configuration of the GPS used: in this one protons have been considered, simulating only one proton per event; protons have been generated from a spherical surface following the energy distribution obtained by the logarithmic interpolation of proton flux included in the file "proton-flux.dat", containing the spectrum model described in sections 5.4.1 and 5.4.2.

```
/run/initialize

/random/setSeeds 1717 2727

/gps/particle proton
/gps/ene/type Arb
/gps/hist/type arb
/gps/hist/file protonflux.dat
/gps/hist/inter Log
/gps/pos/type Surface
/gps/pos/shape Sphere
/gps/pos/centre 0 0 0 m
/gps/pos/radius 801000 cm
/gps/ang/type cos
/gps/ang/mintheta 0 deg
/gps/ang/maxtheta 90 deg
/gps/number 1

/myact/gun/beamTime 10 year

#/myact/geom/file LLchond.gdml
/myact/geom/update

/analysis/setFileName LLchond

/run/printProgress 3000

/run/beamOn 300000000
```

Figure 5.1: Example of one of the configuration file used in this work.

5.3.2 MEGAlib

The other main software used in this work is MEGAlib (the medium Energy Gamma-ray Astronomy library), a simulation and data analysis tool developed by Andreas Zoglauer. The MEGAlib software package is completely written in C++ and it uses the ROOT software library for its graphical user interface and its data display.

It has been developed mainly for the Analysis of Compton and low-energy pair telescopes; originally it has been thought specifically for the MEGA Compton and pair telescope prototype, but it was possible to adapt and expand MEGAlib to different hard X-ray and gamma-ray telescopes [37] – [38].

MEGAlib encompasses the complete data analysis pipeline from simulations to high-level data analysis, which includes:

- the construction of a geometry and detector setup with *Geomega*. Geomega allows the full description of the detector and the geometry file must include the description of all materials, volumes and detector properties of the instruments, such as its energy resolution;

- the interaction of particles and matter is simulated by *Cosima*, and the energy deposited in the various volumes is obtained. Cosima is based on Geant4 and all relevant parameters (range cuts, physics lists) can be set [39];

- the event reconstruction is performed with *Revan*. Energy depositions from the Monte Carlo are corrected accounting for the detector resolution and noise, and the obtained information is analysed to derive the preferred interaction type (photoelectric, Compton, pair production) and the inferred parameters for the primary (measured energy, measured direction, etc.);

- the high-level data analysis with *Mimrec* including, for example, optimized event selections. With Mimrec it is possible to select events on various parameters of Compton and pair events; it provides also analysis of energy spectra and Compton image reconstruction.

For this work we use Cosima and a home-made version of Revan, tweaked to save in ROOT tuples all the available Monte Carlo information and reconstructed parameters, allowing us to easily investigate and apply quality cuts.

```
// Run Cosima to  to determine energy, angular resolution, effectiove area (see Mimrec manual)

// Global parameters:
Version                 1
Geometry                /data/local/analysis/sara/megalib/cube0sipm2-eres/detector.setup
#CheckForOverlaps 10000 0.0001

# Physics list
PhysicsListEM                           Livermore
PhysicsListEMActivateFluorescence       false

# Output formats
StoreCalibrated                         true
StoreSimulationInfo                     true
StoreSimulationInfoIonization           false
DiscretizeHits                          true

#Borders
StoreScientific                         true 5

#Run parameters:
Run TestRun
TestRun.FileName                        600aster-eres
TestRun.Time                            600


TestRun.Source 1_Line
1_Line.ParticleType             1
1_Line.Beam                     FarFieldPointSource 0.0 0.0
1_Line.Spectrum Mono 846.77
1_Line.Flux    0.126


TestRun.Source 1_bk
1_bk.ParticleType               1
1_bk.Beam                       FarFieldPointSource 0.0 0.0
1_bk.Spectrum PowerLaw  524.8   1000                    1.018
1_bk.Flux       15.84
```

Figure 5.2: Example of one of the configuration file used in this work.

In figure 5.2 one example of configuration file for Cosima is shown; it specifies the file containing the geometry of the detector, the physics list for Geant4, the simulated time (10 minutes) and the particle source. Here parallel photons are generated from the zenith coming from 2 sources: one with a line spectrum (E=846.77 keV), the other with a power law spectrum (E_{min}=524 keV, E_{max}=1000 keV, index 1.018).

We use MEGAlib to perform all simulations of the gamma-ray sources, including the asteroid, and to simulate the activation of the detector and satellite due to cosmic protons.

5.4   Radiation Environment

The asteroid is located approximately at Earth's distance from the Sun.

The most relevant species are protons, responsible for the activation of materials and therefore causing a gamma-ray background, and cosmic gamma rays. Alpha and heavier ions add a negligible correction to the effects caused by protons, and electrons are efficiently rejected by the anti-coincidence systems of our detectors: both have been ignored.

Among cosmic sources of gamma rays there are point sources (galactic and extra-galactic) and diffuse components.

Given the estimated sensitivities of our detectors and the lack of a plan for orbit and attitude at this stage, we can ignore the point sources, assuming we align with the target to set the brighter ones away from the line of sight.

In addition to charged particles, it must be considered also the contribution due to the environmental gamma rays.

5.4.1   Galactic protons

Galactic cosmic ray particles are high-energy charged particles that enter the solar system from the outside; their flux is in anti-correlation with the solar activity. They are composed of protons, electrons and fully ionized nuclei. As mentioned before, we will focus only on galactic protons.

Galactic protons are described by several models, but these models do not differ significantly from each other. The main differences between the models are at low energies (see figure 5.3).

The ISO-15390 model is used: this model is based on the semi-empirical galactic cosmic ray models of the Moscow State University; it averages 12 months of sunspot numbers, in order to take into account solar-cycle variations that can affect the intensity of galactic particles. The ISO-15390 model does not take into account anomalous cosmic rays.

5.4.2   Solar protons

The flux of solar protons is the combination of a steady flux, dependent on the activity of the Sun within the solar cycle, and of a series of stochastic events (flares, coronal mass ejections). Models that describe the solar proton flux are therefore stochastic, and the intensity is determined by the confidence level one requires: the true flux will be below the one provided, at the required confidence level.

In this work we use SAPPHIRE [40], accessed through the ESA Spenvis server. We request an "average" flux for the year 2028 by setting the confidence level at 50%, see figure 5.4.
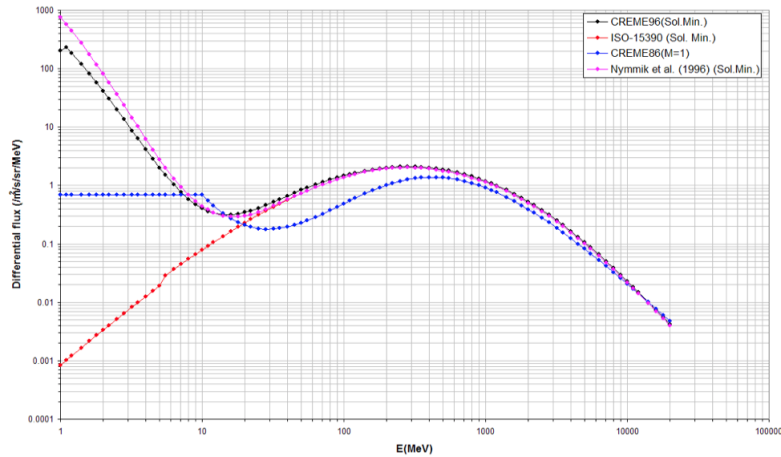
Figure 5.3: Galactic proton flux predicted by different models at solar minimum.
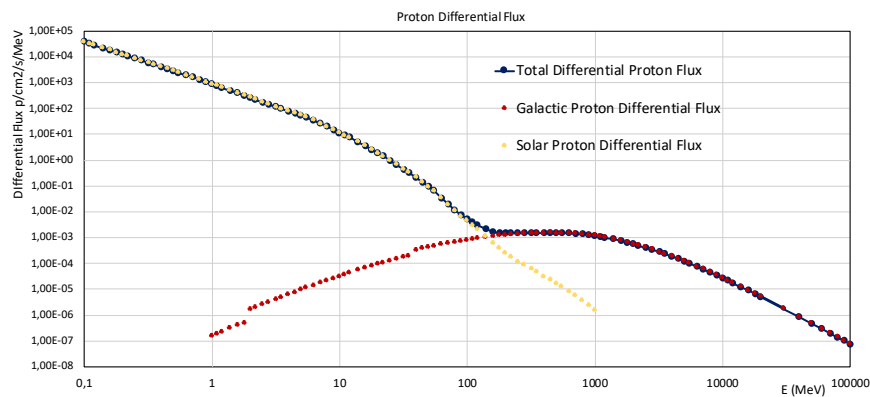
Figure 5.4: Total differential flux of protons.

5.4.3 Environmental gamma rays

In order to perform the simulations with MEGAlib, in addition to the gamma rays produced by the surface asteroid, all the environmental contributions must be considered. The two most important contributions are due to extragalactic background and the diffuse continuum gamma-ray emission from the Galactic plane.

- The extragalactic background (EGB) light is an isotropic and homogeneous background; it is mostly due to unresolved sources.

  It has been measured by several experiments (see figure 5.5); in particular, for the energy range of interest and for the sensitivity of our instruments we refer to results from COMPTEL.

- The diffuse gamma-ray emission from the Galactic plane is due to the interactions of cosmic rays with the interstellar medium (gas, dust and radiation).
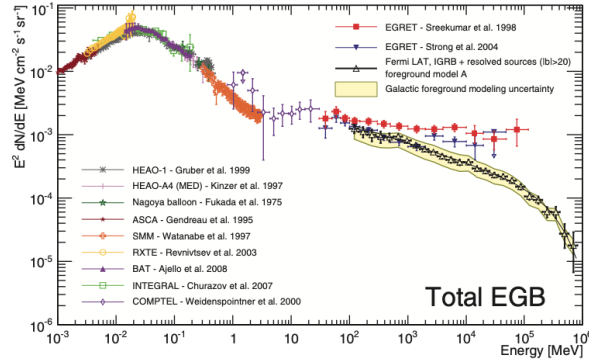
Figure 5.5: Galactic proton flux predicted by different models at solar minimum [42].

We again refer to COMPTEL measurement: from [41] we derive an averaged power-law spectrum with index $\gamma = -2$ and flux Φ=0.25 particles/cm^2/s. For the spatial profile we define an uniform ring at the equator of our instrument (the target is at the zenith) with width σ=5°.

5.5   Material activation

Interactions of energetic particles with the material of the instrument can produce radioactive isotopes, that can generate a significant contribution to the signal collected by the detector. This effects must be taken into account, since it can influence the performance of the instrument.

Clearly, the higher the mass and the heavier the elements, the more this unwanted effect is amplified; in particular, if one considers the mass of the satellite carrying the detector, activation will increase further.

MEGAlib provides an internal tool named "Activation" that simulates in three step the effect of particles with the material of the instruments:

- in the first step MEGAlib simulates primary protons interactions with the materials of the detector; these interactions originate all possible decay chains, that are recorded by the software;

- secondly, the tool calculates material activation, taking into account the time scheduled for the mission;

- finally the software simulates in the desired observational time the detection of gamma rays coming from the material activation, simulated in the second step.

Internally, MEGAlib uses Geant4 for this simulation.

In order to have a consistent picture we tuned our Geant4 simulation to be as close as possible to this, in particular by selecting the appropriate physics lists.

As the MEGAlib documentation recommends, the results should be taken with caution and need to be calibrated with experimental observations.

Chapter 6

Detectors

6.1 Detectors

The detectors we will consider will be Compton cameras, one with a scintillator hodoscopic system, capable of determining position and energy for the first and second Compton interaction, and one with a Si microstrip array, capable of tracking the scattered electron at the first interaction. For comparison we will also consider a scintillator system similar to NEAR.

6.1.1 The tracker

The tracker permits the reconstruction of particles trajectory. A good choice is a finely segmented stack of semiconductor detectors.

We will consider silicon microstrip trackers, since this technology has a great heritage in space mission, e.g. Fermi LAT. Differently from Fermi LAT we will use double sided detectors to minimise electron scattering.

The tracker characteristics are reported in table 6.1.

Layers lateral size	7.4 cm × 7.4 cm
Layers thickness	500 μm
Strips pitch	500 μm
Number of layers	30
Distance between layers	0.2 cm

Table 6.1: Characteristics of the double-sided microstrip trackers.

The read-out electronics is given by the ASIC VATA460 with 32 channels, with 10 bit of digitizations, which gives as energy resolution ∼5 keV from 100 keV up to few MeV, as reported in [43].

In MEGAlib we construct first a single crystal, then we repeat it for 30 times along the z-axis. In the tracker definition we describe also the energy resolution (∼5 keV,

see [43]) and the bias for the centroid of the measured energy distribution (none).

6.1.2   The 3D calorimeter

The calorimeter allows to measure the total energy of electrons and photons by converting the ionization energy release into optical light.

We will consider a 3D calorimeter formed by several thin bars of CsI; the readout is performed on both the ends of each single bar in order to measure the longitudinal position of the energy deposition by the asymmetry of the collected light. The required light yield asymmetry is obtained by scratching one side on the crystal with abrasive paper before wrapping it in reflective foil.

This kind of detector is part of the heritage of other space mission, e.g. Fermi LAT.

Bars are organised into xy modules: each module has an array of 12 bars along the x direction and 12 bars along the y direction.

Calorimeter's characteristics are reported in table 6.1. See for more detail [44].

Single bar size	$0.50 \times 0.50 \times 7.50$ cm^3
Longitudinal resolution	0.5 mm
Bars number in the module	12×12

Table 6.2: Characteristics of the 3D calorimeter.

The light signal is read out by silicon photomultipliers (SiPMs) and again VATA460; with respect to the previous estimates for this detector in [44] the energy resolution has been worsened by a factor ~ 3, in agreement with the experimental results of [45].

In MEGAlib we first assemble a xy module from CsI crystals with cellulose-based wrapping. This module can be placed around and under the Si tracker, or several modules can be stacked in order to have a calorimeter-only cube.

As in the case of the tracker we must define the energy resolution (from 7.5 keV at 100 keV to 33 keV at 2 MeV) and the energy bias (none).

6.1.3   The anticoincidence

The anticoincidence is a scintillator detector configured as a veto. It is the main barrier against charged particle backgrounds and its efficiency is so high that they become a negligible component of the backgrounds (see [46]).

The anticoincidence is designed as a box which completely encloses the detector. Its thickness is 50 mm; the material used is NE110, which is a plastic compound formed by H (84 atoms), C (74 atoms) and O (1 atom); its density is 1.03 g cm^{-3}.

The light signal is read out by silicon photomultipliers (SiPMs) and VATA460, as for the calorimeter.

Again we must define in MEGAlib the energy resolution (10 keV from 1 keV to 10 keV) and the energy bias (none).

6.2   The geometry

With the blocks above we build two Compton cameras, a cheaper one with only CsI crystals and no electron tracking, an a more expensive one with the Si tracker core, to reconstruct the direction of the scattered electron.

6.2.1   Detector 1: tracking Compton camera

In figure 6.1 we show the geometry of the tracking Compton instrument.

It is comprised of the Si tracker core, surrounded on 4 lateral sides and on the bottom by a CsI *xy* calorimeter module; the plastic ACD surrounds all.

In addition we included 4 structural Al bars at the corners.

At this stage we did not include any readout electronics or cabling, so this is clearly an unfeasible design, and we will obtain an overestimate of the performance, for the purpose of comparison with the other designs.
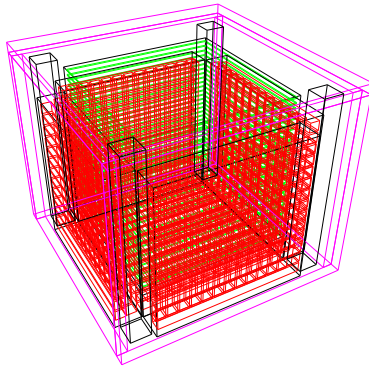
Figure 6.1: Geometry of detector 1.

The material composition of this instrument is found in table 6.3.

Material	Density [g cm^{-3}]	Total mass [g]	Structure
CsI	4.5	1013	calorimeter
Si	2.33	191	tracker
Cellulose	1	160	calorimeter
NE110	1.03	281	anticoincidence
Al	2.7	99	structure bars
Total mass		1744	

Table 6.3: Recap of detector 1 materials.

The trigger system is defined in MEGAlib: we request to have 2 simultaneous hits,

one in the tracker and one in the calorimeter; the trigger thresholds are set to 10 keV and 30 keV, respectively. The anticoincidence is used as a veto, with a trigger threshold of 50 keV.

6.2.2   Detector 2: non-tracking Compton camera

In figure 6.2 we show the geometry of the non-tracking Compton instrument.

It is comprised of a stack of 6 xy calorimeter modules surrounded by the anticoincidence. Here we have not included any additional structural elements.

Again a warning, at this stage we have not included any readout electronics or cabling, so this is will give us an overestimate of the performance, but it is appropriate for a comparison of the different designs.
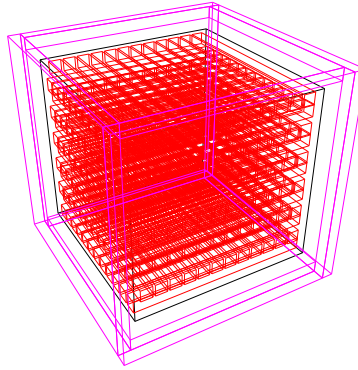
Figure 6.2: Geometry of detector 2.

The material composition of this instrument is found in table 6.4.

Material	Density [$\mathrm{g\,cm^{-3}}$]	Total mass [g]	Structure
CsI	4.5	1215	calorimeter
Millipore	1	163	calorimeter
NE110	1.03	241	anticoincidence
Total mass		1619	

Table 6.4: Recap of detector 2 materials.

The trigger system is defined in MEGAlib, we request to have 2 simultaneous hits in the calorimeter and the trigger threshold is set to 30 keV. The anticoincidence is used as a veto, with a trigger threshold of 50 keV.

6.2.3 Detector 3: scintillator system

For reference we create an instrument as similar as possible as the NEAR detector: a core NaI cylinder and an outer cylindrical BGO shield.

Once again we ignore the readout, so not even the PMTs are implemented.

The geometry of this detector is shown in figure 6.3.
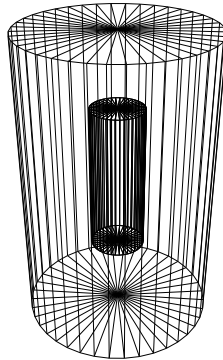
Figure 6.3: Geometry of detector 3.

- The NaI core is a cylinder of radius 1.27 cm and of height 7 cm. Its energy resolution is 58 keV at 662 keV and 95 keV at 2 MeV.

- The BGO shield is a cylinder of radius 4.45 cm and of height 24 cm, which envelopes the NaI core. Its energy resolution is 92 keV at 662 keV and 152 keV at 2 MeV.

The material composition of this instrument is shown in table 6.5.

Material	Density [$\mathrm{g\,cm^{-3}}$]	Total mass [g]	Structure
NaI	3.67	130.173	inner scintillator
BGO	7.1	5930.607	outer scintillator
Total mass		6060.780	

Table 6.5: Recap of detector 3 materials.

As mentioned in section 4.1 we cannot replicate the escape-peak tag readout used in NEAR [47] in MEGAlib, so we operate in a more naive way, requesting 30 keV for a trigger in the core, and using the shield as veto with a threshold of 30 keV.

6.3   Satellite

The detector will be placed on a satellite, occulting some diffuse gamma rays from the back and in particular adding to the backgrounds due to material activation.

To evaluate this effect we will add a very simple structure, as seen in figure 6.4 for the first detector.
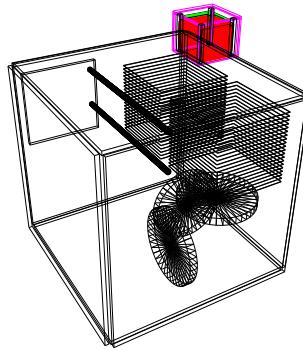
Figure 6.4: Satellite and Detector 1 geometry.

The satellite is composed by an Aluminum box, containing several circuit boards, three Iron disk (reaction wheels) and Copper plate and tubes (thermal control).

The mass breakdown, for the first detector, is reported in table 6.6.

Material	Density $[\mathrm{g\,cm^{-3}}]$	Total mass [g]
Silicon	2.33	191
Steel	7.87	14686
Circuit Board	1.8	2880
Copper	8.954	3829
CsI	4.5	1013
Millipore	1	160
NE110	1.03	281
Aluminum	2.7	40583
Total mass		63623

Table 6.6: Recap of detector 1 and satellite materials.

Chapter 7

Analysis and results

7.1 Simulations of primary protons

Primary protons have been considered as the only particles interacting with the surface of the asteroid.

1. We take the proton spectrum described in section 5.4 and the asteroid, which is the target of these protons, as described in section 5.2.

2. We generate 3×10^8 primary protons, requiring an affordable amount of CPU hours. This number sets the statistical uncertainties, which are less severe than systematical uncertainties.

3. Primaries are generated isotropically from a spherical surface surrounding the asteroid barely above the surface. In figure 7.1 it is possible to see the energy spectrum of protons simulated by Geant4.
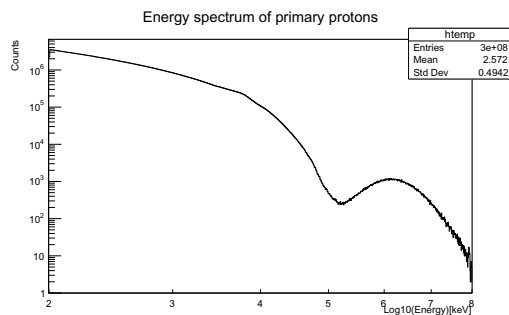
Figure 7.1: Energy spectrum of primary protons simulated with Geant4.

4. We generate the protons randomly in a time interval of 10 years, and all products of interactions and decays are stored.

5. We then consider only gamma rays escaping from the asteroid in the second half of the total time simulated (see figure 7.2): in this way isotopes half-lives of 1 year or less are at dynamical equilibrium. In figure 7.3 isotopes created by the interaction of protons in this time interval are shown.
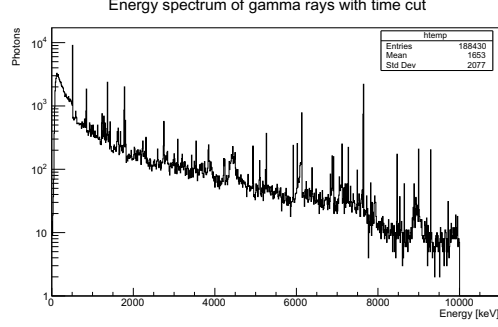
Figure 7.2: Energy spectrum of gamma rays from the asteroid's surface with the time cut.
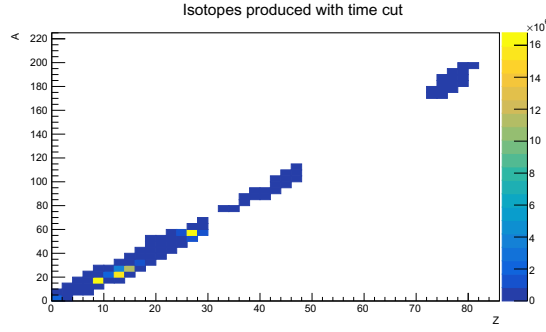
Figure 7.3: Isotopes present in the asteroid with time cut.

7.2   Characteristic lines flux

We analyse a few selected lines relevant for the classification of the asteroid's composition. For each line we will simulate the observation with our detectors with MEGAlib.

To derive the input flux we proceed as follows:

1. we take the entire gamma flux from the Geant4 simulation, irregardless of the gamma direction ;

2. we select an energy window around the selected line much larger than the energy resolution of the detectors;

3. we count the photons in any line in the window, N_γ^{obs}, and we fit the continuum with a power law;

4. we convert the counts into fluxes Φ_γ in particles/s/cm^2 at the distance of the detector taking into account some correction factors. In particular:

$$\Phi_\gamma = \frac{N_\gamma^{obs}}{T^{obs}} \cdot \frac{1}{4\pi d^2} \cdot \frac{N_{true}}{N_p} \qquad (7.1)$$

where T^{obs} is the time length observed (T^{obs}= 5 years), d represents the distance between the asteroid and the detector (d=35 km), N_p is the number of primary protons simulated by Geant4 (N_p=3·10^8 protons).

We define N_{true}, which is the number of protons we should have simulated in T^{sim}, as:

$$N_{true} = \Phi_p \cdot T^{sim} \cdot 4\pi r^2 \qquad (7.2)$$

where r is the radius from which primary protons are generated (r=8.01 km), Φ_p is the flux of primary protons in our model, in protons/cm^2/s and T^{sim} is the time length simulated by Geant4 (T^{sim}= 10 years).

We do not simulate the angular distribution of incident photons on our detector (they are parallel to each other), but the performance of the instrument depends very little on the incidence angle (see [46]). On purpose we refrain from applying event selection cuts based on the reconstructed direction of the gamma rays, leaving room for further improvements.

We will focus on the analysis of the Fe and Si characteristic lines, which were also the focus of the analyses of the NEAR mission.

7.3 Effective area simulations

To have a simple numerical estimate of the relative performance of the detectors for line detection we estimate the effect of efficiency and energy reconstruction.

We simulate with MEGAlib monochromatic point sources at energies corresponding to the chosen lines, and we evaluate the effective area: effective area is the detector efficiency in units of cm^2 and converts input fluxes into observed counts.

The source beam has been generated from a FarFieldPointSource, in which particles are emitted by a disk of radius 15 cm.

With some ROOT analysis we estimate the effective area of our detector.

1. We start with the flux of simulated events, Φ_{tot}.

2. We have a number of detected events, with successful trigger and event reconstruction.

3. A fraction of these events will have a bad energy reconstruction and will end up in the continuum spectrum. We fit the "good" events with a Gaussian around the true energy and measure the number of events reconstructed in the line, N_{gauss}.

4. We calculate the effective area, A_{eff}, for line observations as:

$$A_{eff} = \frac{N_{gauss}}{\Phi_{tot}} \qquad (7.3)$$

In addition to this, we can apply quality cuts, to reject event classes with a bad signal-to-noise ratio. This lowers the effective area and thus the event count rate, but it will improve the uncertainties on the line measurements.

7.4   Detector 1: tracking Compton camera

7.4.1   Effective area

Monochromatic sources of energy 847 keV and 1779 keV, for Fe and Si respectively, have been simulated, as described in section 7.3.

There are some unphysical events that we have not considered and so we exclude them from our analysis. These are the event cuts we found improving the signal-to-noise ratio by proportionally reducing the activation component:

- the electron is going backward, since asteroid is in front of the instrument,

- the Compton angle is > 1 rad,

- the second Compton has gamma energy, E_γ, not in 467–562 keV.

We report in table 7.1 the value of the effective area for the first detector: these cuts reduce the effective area of the detector. In the third column of table 7.1 there is reported the activation value, calculated as the number of activation events that remain after the cuts, normalised to the number of activation events without any cut.

Energy [keV]	A_{eff} [cm^2]	Activation [a.u.]	Mode
847	1.85	1	without restrictions
847	0.58	0.06	with cuts
1779	0.74	1	without restrictions
1779	0.19	0.06	with cuts

Table 7.1: Effective area values for detector 1.

The gain in signal-to-noise ratio thanks to the quality cuts is clear.

7.4.2   Fe and Si components

In the next sections, by deriving the intensity of the Fe (847 keV) and Si (1779 keV) lines (see for more detail [48]) we can estimate our sensitivity to the concentration of said elements.

Notably in our simulation there is a second line due to Si close to the reported one, not resolvable with our resolution, which contributes in a significant way to the energy spectrum of gamma-rays.

Fluxes are reported in table 7.2.

So simulations of one month of the Fe signal and Si signal, originating from the asteroid, have been performed with MEGAlib.

Type	Energy [keV]	N_γ	Φ_γ [particles/s/cm^2]
line Fe	847	1235	$2.54{\cdot}10^{-3}$
line Si	1779	1743	$3.59{\cdot}10^{-3}$
line Si	1808	1070	$2.20{\cdot}10^{-3}$
background	700–1000	12400	$2.55{\cdot}10^{-2}$
background	1400–2200	17940	$3.69{\cdot}10^{-2}$

Table 7.2: Parameters for MEGAlib source files for Fe and Si components used for detector 1.

7.4.3 Observed Fe counts in 30 days

We perform a simulation of 30 days of observation. The same physical cuts, already used to calculate the effective area, have been considered.

This output has been analysed with ROOT, in particular it has been fitted with a power law and a Gaussian function. The result of this is visible in fig 7.4.
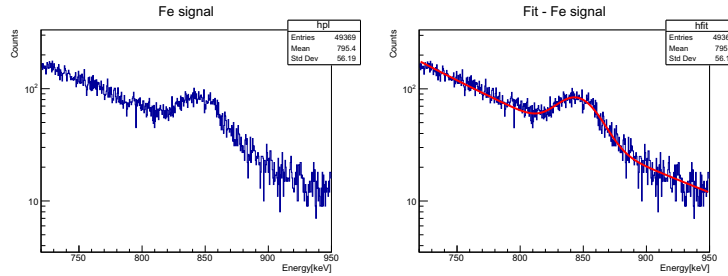
Figure 7.4: Fe signal analysis for detector 1.

7.4.4 Observed Si counts in 30 days

We perform a simulation of 30 days of observation. The same physical cuts, already used to calculate the effective area, have been considered.

As for the Fe signal, the output has been analysed with ROOT, in particular it has been fitted with a power law and a Gaussian function.

As mentioned in 7.4.2, in our activation simulation the Si line is actually a doublet, see figure 7.5.
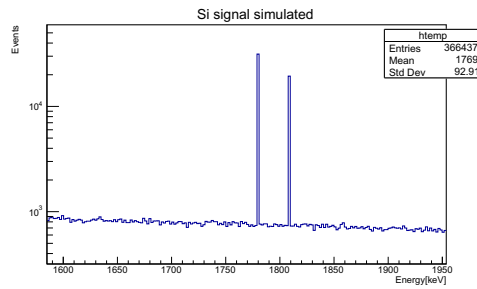
Figure 7.5: Si signal (as simulated).

The corresponding observation is shown in figure 7.6; given our resolution the doublet is fit with a single gaussian.
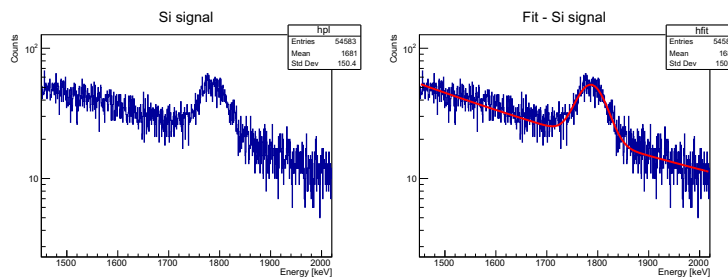
Figure 7.6: Si signal analysis for detector 1.

7.4.5   Observed EGB counts in 30 days

With the same cuts made for the Fe and Si signal, one month of the EGB radiation has been simulated. The outcome of this simulation is shown in figure 7.7.
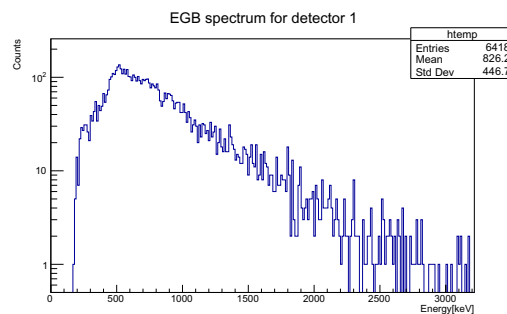
Figure 7.7: EGB background for detector 1.

7.4.6 Observed diffuse Galactic counts in 30 days

With the same cuts made for the Fe and Si signal, one month of the galactic diffuse radiation has been simulated. The outcome of this simulation is shown in figure 7.8.
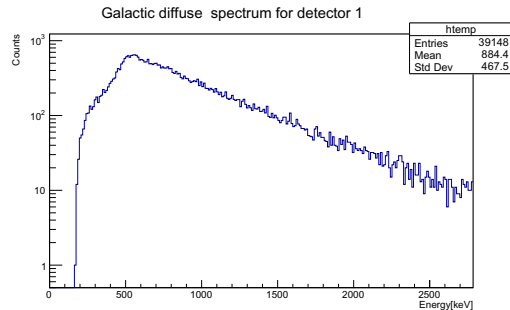
Figure 7.8: Galactic diffuse background for detector 1.

7.4.7 Observed activation counts in 30 days

The activation is calculated using the dedicated tool of MEGAlib (see section 5.5).

Since the simulations take a lot of time, we simulate only 10 days; then, in order to compare different data in the same amount of time, we multiply these activation data for a factor 3, obtaining one month of observation.

The material activation spectrum for the original 10 days simulated is shown 7.9.
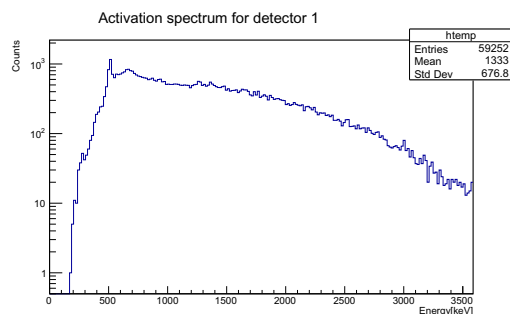
Figure 7.9: 10 days activation background spectrum for detector 1.

This activation is only due to the materials of the detector.

7.4.8 Observed satellite activation counts in 30 days

As for the previous point, we decided to simulate 10 days and then we multiplied the result for a factor 3; figure 7.10 shows the material activation spectrum for the original 10 days simulated.
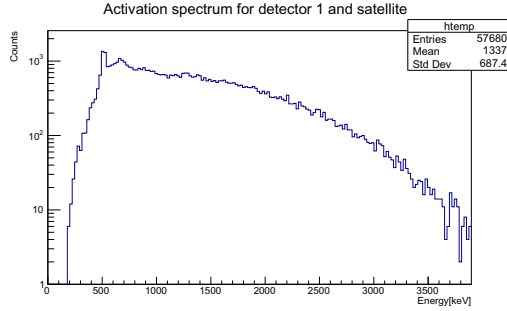
Figure 7.10: 10 days activation background spectrum for detector 1 and satellite.

7.4.9   Results for detector 1

We remark that the total time of observation of our asteroid is one month (only in the case of the activation we simulate a shortest period and then we multiply it). All data have been taken with the same physical cuts, in order to make our result coherent.

We follow these steps during the analysis.

- First we have summed the several components: the signal, the EGB signal, the Galactic diffuse signal, the activation (with or without the satellite). We obtain a cumulative spectrum.

- Then we apply a power law fit to the background and a gaussian fit to the signal expected. In particular, since the characteristic energy of the wanted line is known, we fix the mean parameter of the Gaussian, which corresponds to the energy.

- From the Gaussian area, taking into account the normalisation factor due to the bins width, we find the number of photon that correspond to the presence of the wanted element.

Fe signal

The analysis just described for the Fe signal and the detector without the satellite is reported in figure 7.11; the black line represents the cumulative signal, the red line is the Fe signal without any source of backgrounds.

It must be noticed that two of the components of the background, which are the galactic diffuse component (light blue line) and the EGB (blue line), are quite negligible with respect to the background caused by the detector activation.

Moreover, the activation (green line) has a significant role, but it does not affect too much the performance of the instrument in this energy range.

In table 7.3, the parameters of the final fit, from which we can find out the number of photon that our first detector would see in one month of observation, are reported. In particular the parameter γ indicates the slope of the power law, while σ indicates the standard Gaussian parameter. The number of photons has been found from the normalised Gaussian area. We report also the χ^2 value of the fit.
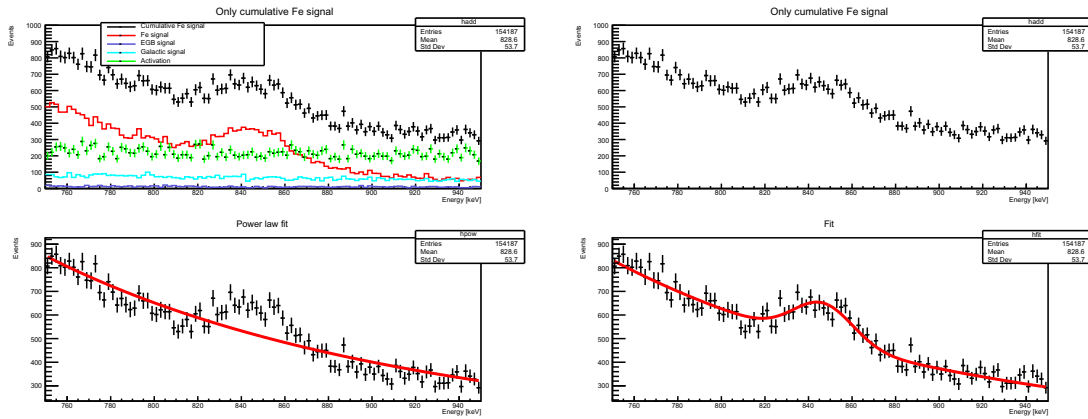
Figure 7.11: 1 month of Fe spectrum for Detector 1.

γ	E_{line} [keV]	σ [keV]	χ^2/dof	Photons
$(-440.6 \pm 9.6)10^{-2}$	846.77	$(137.3 \pm 9.7)10^{-1}$	108.4/96	$(28.2 \pm 2.2)10^2$

Table 7.3: Fit parameter for Fe signal of detector 1.

In conclusion, we observe the line with a signal-to-noise ratio of 12.8 for a nominal Fe mass abundance of 3.79%, so we are sensitive to abundance of roughly 4.27 times inferior (corresponding to 3σ signal-to-noise ratio).

We then repeat the same procedure for the detector and satellite, always looking at the 846.77 keV line coming from Fe. In figure 7.12 there is the cumulative signal and its fit analysis, while the fit parameters are presented in table 7.4.

γ	E_{line} [keV]	σ[keV]	χ^2/dof	Photons
$(-439.2 \pm 9.6)10^{-2}$	846.77	$(124.5 \pm 8.7)10^{-1}$	105.6/96	$(28.7 \pm 2.2)10^2$

Table 7.4: Fit parameter for Fe signal of detector 1 and satellite.

It is clear that activation in the detector is the main background source, and that addition of the spacecraft changes very little.

In conclusion, including the effect of the satellite, we observe the line with a signal-to-noise ratio of 13.0 for a nominal Fe mass abundance of 3.79%, so we are sensitive to abundances of roughly 4.35 times inferior (corresponding to 3σ signal-to-noise ratio).

Pleas note that we have applied the event selection cuts in section 7.4.1; in particular we are not applying any cut on the reconstructed incoming direction of the photons.
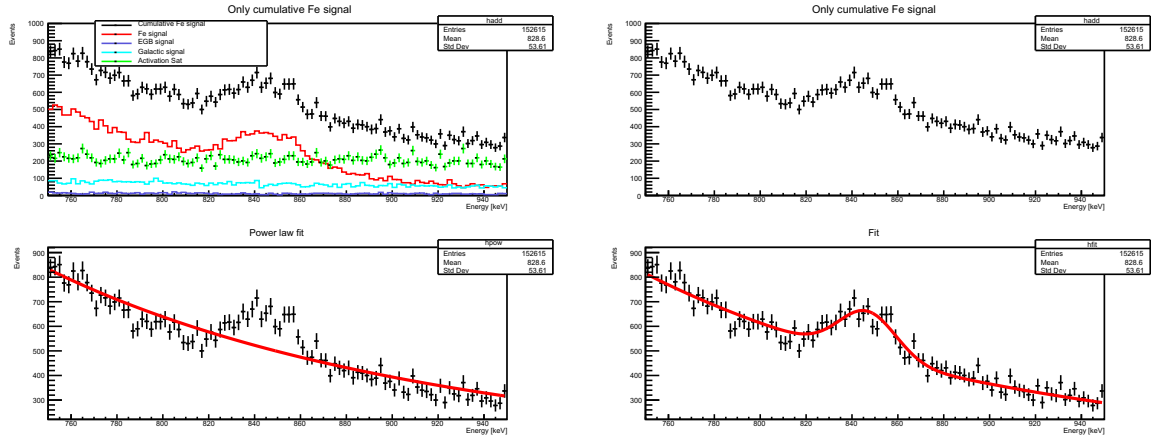
Figure 7.12: 1 month of Fe spectrum for detector 1 and satellite.

Si signal

We then repeat the same analysis for the Si line at an energy of 1779 keV. We report here only the graphical result for the case without the satellite (see figure 7.13).
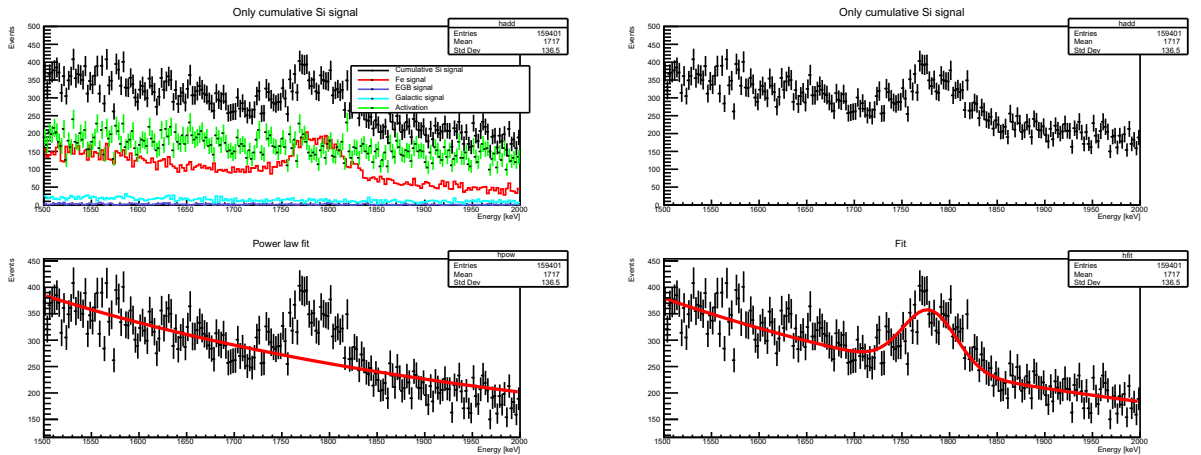
Figure 7.13: 1 month of Si spectrum for detector 1.

In table 7.5 the results of the fit analysis for the Si signal without the satellite are reported.

In conclusion, we observe the line with a signal-to-noise ratio of 13.4 for a nominal Si mass abundance of 19.45%, so we are sensitive to abundances of roughly 4.48 times inferior (corresponding to 3σ signal-to-noise ratio).

In table 7.6 the results of the fit analysis for the Si signal with the satellite 7.6 are reported.

It is clear that activation in the detector is the main background source, and that

γ	E_{line} [keV]	σ [keV]	χ^2/dof	Photons
$(-252.7 \pm 8.1)10^{-2}$	1779	(28.0 ± 2.0)	234.5/196	$(30.9 \pm 2.3)10^2$

Table 7.5: Fit parameter for Si signal of detector 1.

γ	E_{line} [keV]	σ [keV]	χ^2/dof	Photons
$(-246.0 \pm 8.1)10^{-2}$	1779	(27.0 ± 2.4)	260.1/196	$(30.0 \pm 2.4)10^2$

Table 7.6: Fit parameter for Si signal of detector 1 and satellite.

addition of the spacecraft changes very little.

In conclusion, including the effect of the satellite, we observe the line with a signal-to-noise ratio of 12.5 for a nominal Si mass abundance of 19.45%, so we are sensitive to abundances of roughly 4.17 times inferior (corresponding to 3σ signal-to-noise ratio).

Pleas note that we have applied the event selection cuts in section 7.4.1; in particular we are not applying any cut on the reconstructed incoming direction of the photons.

7.5 Detector 2: non-tracking Compton camera

7.5.1 Effective area

Monochromatic sources of energy 847 keV and 1779 keV, for Fe and Si respectively, have been simulated, as described in section 7.3.

There are some unphysical events that we have not considered and so we exclude them from our analysis. These are the event cuts we found improving the signal-to-noise ratio by proportionally reducing the activation component:

- the first Compton hit has energy greater than 140 keV and not in 460–560 keV,

- the second Compton has scattered gamma energy not in 170–210 keV, or not in 340–410 keV, or not in 470–540 keV or not in 680–720 keV,

- the Compton angle is not between 0.15–0.55 rad.

We report in table 7.7 the value of the effective area for the second detector: as it is possible to see these cuts reduce the effective area of the detector. In the third column of table 7.7 there is reported the activation value, calculated as the number of activation events that remain after the cuts, normalised to the number of activation events without any cut.

The gain in signal-to-noise ratio thanks to the quality cuts is clear.

Energy [keV]	A_{eff} [cm^2]	Activation [a.u.]	Mode
846	2.06	1	without restrictions
846	2.11	0.09	with cuts
1779	1.26	1	without restrictions
1779	1.27	0.09	with cuts

Table 7.7: Effective area values for detector 2.

7.5.2   Fe and Si components

In the next sections, by deriving the intensity of the Fe (847 keV) and Si (1779 keV) lines (see for more detail [48]) we can estimate our sensitivity to the concentration of said elements.

Notably in our simulation there is a second due to Si close to the reported one, not resolvable with our resolution, which contributes in a significant way to the energy spectrum of gamma-rays.

Fluxes are reported in table 7.2.

So simulations of one month of the Fe signal and Si signal, originating from the asteroid, have been performed with MEGAlib.

7.5.3   Observed Fe counts in 30 daysl

We perform a simulation of 30 days of observation. The same physical cuts, already used to calculate the effective area, have been considered.

This output has been analysed with ROOT, in particular it has been fitted with a power law and a Gaussian function. The result of this is visible in fig 7.14.
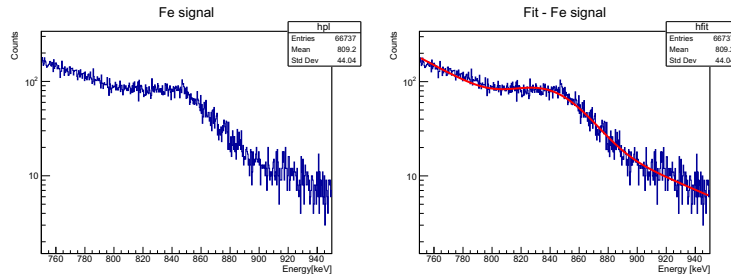
Figure 7.14: Fe signal analysis for detector 2.

7.5.4   Observed Si counts in 30 days

We perform a simulation of 30 days of observation. The same physical cuts, already used to calculate the effective area, have been considered.

As for the Fe signal, the output has been analysed with ROOT, in particular it has been fitted with a power law and a Gaussian function.

As mentioned in 7.5.2, in our activation simulation the Si line is actually a doublet. The corresponding observation is shown in figure 7.15; given our resolution the doublet is fit with a single gaussian.
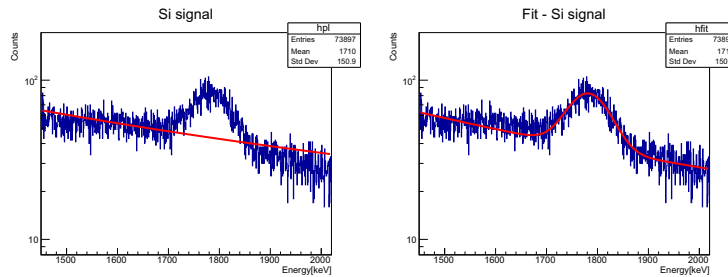
Figure 7.15: Si signal analysis for detector 2.

7.5.5 Observed EGB and diffuse Galactic counts in 30 days

With the same cuts made for the Fe and Si signal, also one month of the EGB radiation and of the galactic diffuse background has been simulated.

For shortness we do not report here the plots of these.

7.5.6 Observed activation counts in 30 days

The activation is calculated using the dedicated tool of MEGAlib (see section 5.5). Since the simulations take a lot of time, we simulate only 10 days; then, in order to compare different data in the same amount of time, we multiply these activation data for a factor 3, obtaining one month of observation.

Figure 7.16 shows the material activation spectrum for the original 10 days simulated.
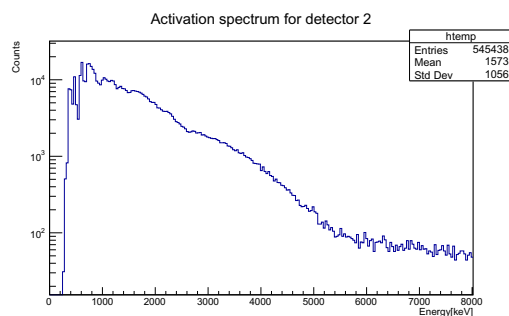
Figure 7.16: 10 days activation background spectrum for detector 2.

This activation is only due to the materials of the detector.

7.5.7 Observed satellite activation counts in 30 days

As for the previous point, we simulate 10 days and then we multiply the result for a factor 3; the material activation spectrum with the satellite for the original 10 days simulated is shown in 7.17 .
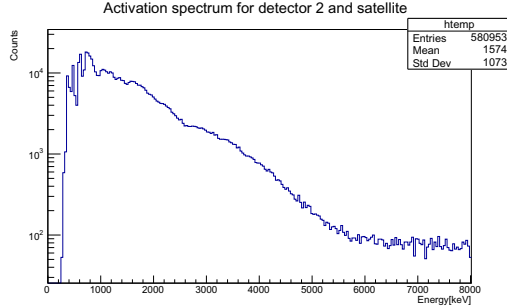
Figure 7.17: 10 days activation background spectrum for detector 2 and satellite.

7.5.8 Results for detector 2

The analysis procedure has been the same than the first detector (see section 7.4.9). We remark that the total time of observation of our asteroid is one month.

Fe signal

In figure 7.18 it is possible to see the result for the analysis for the Fe signal and the detector without the satellite; the black line represents the cumulative signal, the red line is the Fe signal without any source of backgrounds.

It must be noticed that two of the components of the background, which are the galactic diffuse component (light blue line) and the EGB (blue line), are quite negligible with respect to the background caused by the detector activation.

Moreover, the activation (green line) has a more significant role with respect to the first detector.

In table 7.8 the parameters of the final fit, from which we can find out the number of photon that our second detector would see in one month of observation, are reported.

γ	E_{line} [keV]	σ [keV]	χ^2/dof	Photons
$(-454.8 \pm 3.7)10^{-2}$	846.77	$(153.2 \pm 6.9)10^{-1}$	615.8/143	$(91.4 \pm 4.5)10^2$

Table 7.8: Fit parameter for Fe signal of detector 2.

In conclusion, we observe the line with a signal-to-noise ratio of 20.3 for a nominal Fe mass abundance of 3.79%, so we are sensitive to abundances of roughly 6.7 times inferior (corresponding to 3σ signal-to-noise ratio).
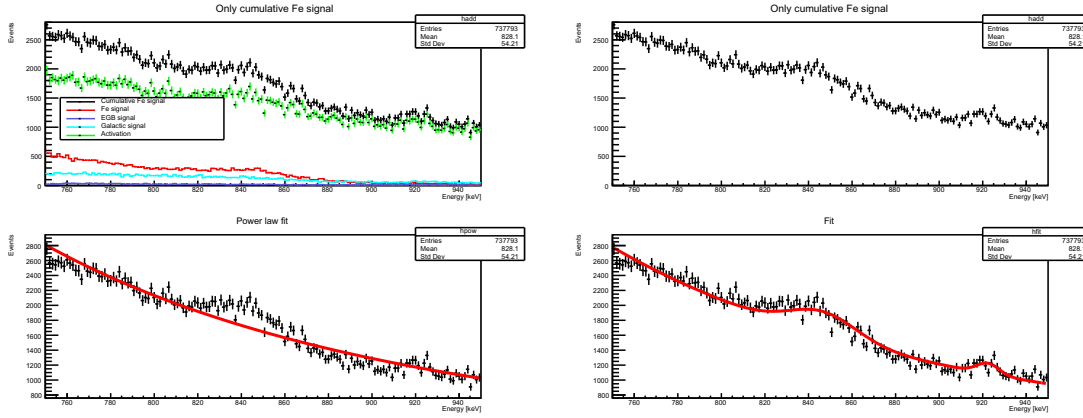
Figure 7.18: 1 month of Fe spectrum for detector 2.

We then repeat the same procedure for the detector and satellite, always looking at the 846.77 keV line coming from Fe. The fit parameters are presented in table 7.9.

γ	E_{line} [keV]	σ [keV]	χ^2/dof	Photons
$(-462.4 \pm 93.7)10^{-2}$	846.77	$(124.5 \pm 5.8)10^{-1}$	718.5/143	$(86.4 \pm 4.1)10^2$

Table 7.9: Fit parameter for Fe signal of detector 2 and satellite.

It is clear that activation in the detector is the main background source, and that addition of the spacecraft changes very little.

In conclusion, including the effect of the satellite, we observe the line with a signal-to-noise ratio of 21.1 for a nominal Fe mass abundance of 3.79%, so we are sensitive to abundances of roughly 7.02 times inferior (corresponding to 3σ signal-to-noise ratio).

Pleas note that we have applied the event selection cuts in section 7.5.1; in particular we are not applying any cut on the reconstructed incoming direction of the photons.

Si signal

We then repeat the same analysis for the Si line at an energy of 1779 keV.

We report here only the graphical result for the case without the satellite, see figure 7.19.

In table 7.10 the results of the fit analysis for the Si signal without the satellite are reported.

In conclusion, we observe the line with a signal-to-noise ratio of 31.3 for a nominal Si mass abundance of 19.45%, so we are sensitive to abundances of roughly 10.4 times inferior (corresponding to 3σ signal-to-noise ratio).

In table 7.11 the results of the fit analysis for the Si signal with the satellite are reported.
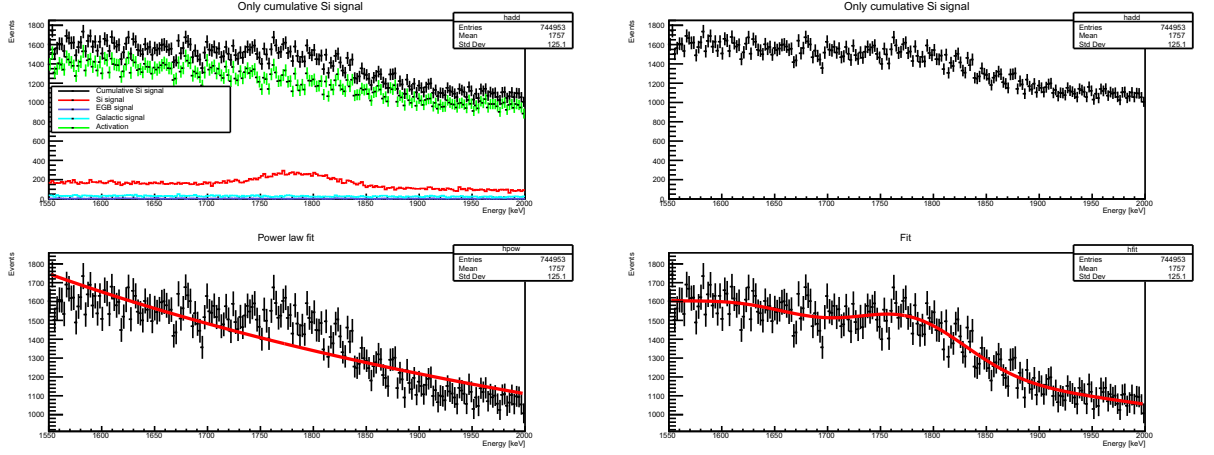
Figure 7.19: 1 month of Si spectrum for detector 2.

γ	E_{line} [keV]	σ [keV]	χ^2/dof	Photons
$(-14.7 \pm 6.3)10^{-1}$	1779	(53.6 ± 4.2)	180.2/193	$(150.0 \pm 4.8)10^2$

Table 7.10: Fit parameter for Si signal of detector 2.

It is clear that activation in the detector is the main background source, and that addition of the spacecraft changes very little.

As it is possible to see from the graphs, activation became more important than for the first detector.

In conclusion, including the effect of the satellite, we observe the line with a signal-to-noise ratio of 17.1 for a nominal Si mass abundance of 19.45%, so we are sensitive to abundances of roughly 5.7 times inferior (corresponding to 3σ signal-to-noise ratio).

Pleas note that we have applied the event selection cuts in section 7.5.1; in particular we are not applying any cut on the reconstructed incoming direction of the photons.

7.6   Detector 3: scintillator system

With this detector it is not possible to analyse data from Compton scattering: for this reason we have to rely on the total energy release in the core scintillator.

For this reason we look at Fe and Si lines at different energies to have the best possible efficiency. Looking at all detectable lines we will focus on the lines at 7631 keV (Fe) and 4934 keV (Si).

γ	E_{line} [keV]	σ [keV]	χ^2/dof	Photons
$(-188.2 \pm 5.4)10^{-2}$	1779	(51.1 ± 2.4)	453.4/193	$(142.0 \pm 8.3)10^2$

Table 7.11: Fit parameter for Si signal of detector 2 and satellite.

7.6.1 Effective area

One of the consequences of analysing data with a single-hit feature is that is not possible to apply some physical cuts to reduce the activation component.

The values of the effective area, obtained with the same procedure of the previous detectors, are reported in table 7.12.

Energy [keV]	A_{eff} [cm^2]
7631	$1.68 \cdot 10^{-2}$
4934	$4.66 \cdot 10^{-2}$

Table 7.12: Effective area values for the detector 3.

From the values we see that in these conditions the effective area is quite low with respect to the more complex Compton cameras.

7.6.2 Fe and Si components

In the next sections, by deriving the intensity of the Fe (7631 keV) and Si (4934 keV) lines (see for more detail [48]) we can estimate our sensitivity to the concentration of said elements.

Notably in our simulation there are other lines due to Si and Fe close to the reported ones, not resolvable with our resolution, which contribute in a significant way to the energy spectrum of gamma-rays.

Fluxes are reported in table 7.13.

So simulations of one month of the Fe signal and Si signal, originating from the asteroid, have been performed with MEGAlib.

7.6.3 Observed Fe and Si counts in 30 days

We perform a simulation of 30 days of observation.

No cuts have been made, since there are not enough available informations to do them.

These outputs have been analysed with ROOT, following the same analysis procedure than the previous detectors.

Type	Energy [keV]	Φ_γ [particles/s/cm^2]
line Si	4934	$3.74 \cdot 10^{-4}$
line Si	5102	$2.53 \cdot 10^{-4}$
line Si	5269	$6.58 \cdot 10^{-4}$
background	4500–5700	$1.23 \cdot 10^{-2}$
line Fe	7631	$1.47 \cdot 10^{-3}$
line Fe	7646	$4.50 \cdot 10^{-3}$
background	700–8500	$7.76 \cdot 10^{-3}$

Table 7.13: Parameters for MEGAlib source files for Fe and Si components used for detector 3.

In this case the signals are not as visible as in detector 1 and 2: this is mainly due to the fact that the fluxes of gamma rays of those energies, coming from the asteroid's surface, are really low.

7.6.4   Observed EGB counts in 30 days

We perform a simulation of 30 days of observation.

No cuts have been made, since there are not enough available informations to do them.

Figure 7.20 shows the outcome of this simulation.
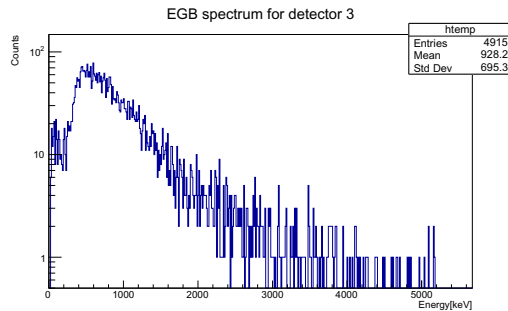
Figure 7.20: EGB background for detector 3

7.6.5   Observed diffuse Galactic counts in 30 days

We perform a simulation of 30 days of observation. Figure 7.21 shows the outcome of this simulation.

7.6.6   Observed activation counts in 30 days

The activation is calculated only without the satellite: in fact, since the signal is really weak, it would have been totally suppressed by the material activation due to the
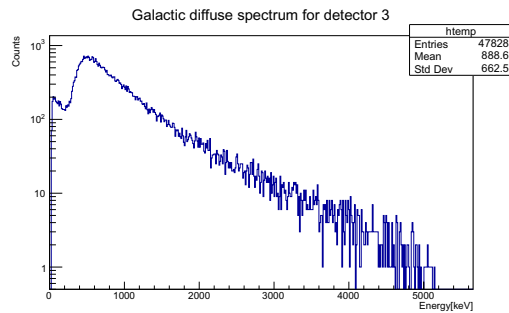
Figure 7.21: Galactic background for detector 3.

satellite.

The activation is calculated using the dedicated tool of MEGAlib (see section 5.5).

Since the simulations take a lot of time, we simulate only 10 days; then, in order to compare different data in the same amount of time, we multiply these activation data for a factor 3, obtaining one month of observation.

The material activation spectrum for the original 10 days simulated is shown in figure 7.22.
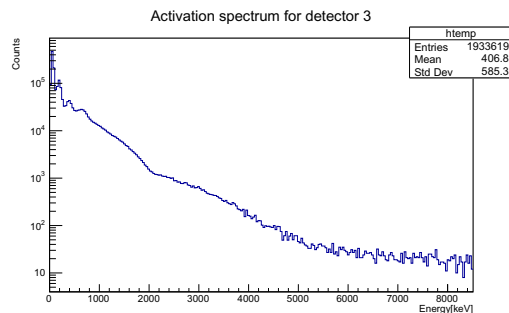
Figure 7.22: 10 days activation background spectrum for detector 3.

7.6.7 Results for detector 3

The analysis procedure is the same of the previous detectors, the only difference is making use of single-hit events.

We remark that the total time of observation of our asteroid is one month and all data have been taken without any quality cuts.

Fe signal

In figure 7.23 there is the result of the analysis for the Fe signal at 7631 keV; the black line represents the cumulative signal, the red line is the Fe signal without any source of backgrounds.

It must be noticed that two of the components of the background, which are the galactic diffuse component (light blue line) and the EGB (blue line), are extremely suppressed respect to the other signals.

Activation has a more important role in comparison with the previous detectors.
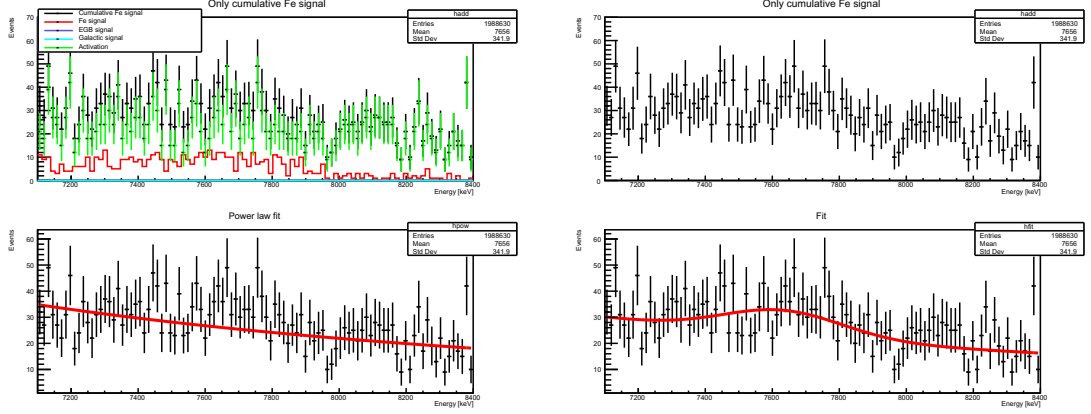
Figure 7.23: 1 month of Fe spectrum for detector 3.

In table 7.14 the parameters of the final fit, from which we can find out the number of photon that our third detector would see in one month of observation, are reported.

γ	E_{line} [keV]	σ [keV]	$\chi^2/$dof	Photons
$(-36.6 \pm 7.5)10^{-1}$	7631	$(18.0 \pm 6.3)10^1$	79.4/96	(33.5 ± 14.6)

Table 7.14: Fit parameter for Fe signal of detector 3.

Under these prohibitive conditions it is clear how with the simulated concentration the abundance of Fe cannot be determined at the 3σ level.

Si signal

We repeat the same procedure also for the Si signal at 4934 keV. We report only the results of the fit analysis in table 7.15.

γ	E_{line} [keV]	σ [keV]	$\chi^2/$dof	Photons
$(-49.9 \pm 4.1)10^{-1}$	4934	(4.6 ± 1.8)	114.6/96	(46.3 ± 23.0)

Table 7.15: Fit parameter for Si signal of detector 3.

Under these prohibitive conditions it is clear how with the simulated concentration the abundance of Si cannot be determined at the 3σ level.

7.7 Precious metals: Pt

We have also tried to find the presence of precious metals in our asteroid. We analyse the signal due to the abundance of Pt with the first detector, since it is the instrument which has the best performances.

- First of all we check if the spectrum of gamma rays coming from the asteroid shows the presence of characteristic lines of Pt. These lines are too weak and they are usually located in regions in which they are near to a lot of other well defined lines. This even before factoring in the performance of our instruments, so there is no point in simulating the observation.

- Since we cannot not find signals of Pt in our analysis, we try to multiply the abundance of Pt in our asteroid. We have simulated until 100 times the initial platinum abundance. Even with such an unrealistic abundance of Pt we do not find any clear evidence of Pt when observed with our first instrument, so we conclude that this measurement is not feasible.

7.8 Radioactive isotopes

Gamma rays coming from the asteroid's surface may be due also to the presence of naturally relic radioactive isotopes, e.g. Th and U.

We do not include them in the composition of our asteroid but the corresponding missing lines are not at energies where they could affect the results above.

Chapter 8

Conclusions

In this work we have shown that it is possible to study the composition of an asteroid using gamma-ray remote sensing through Compton cameras.

With Geant4 and MEGAlib simulations, we simulated the measurement of the abundance of Fe and Si in a stony asteroid with three different detectors. While all the instruments could see the presence of Fe and Si, the difference in performance is clear.

- A simple scintillator system similar to the one on board NEAR could not see the signal with a signal-to-noise ratio of 3. However, NEAR demonstrated better results thanks to a specific data selection (escape-peak) which we could not replicate in our simulations with MEGAlib.

- The non-tracking Compton camera improved the results respect to the scintillator system detector. With some quality cuts we could improve the performance until we saw both Fe and Si lines with very good signal-to-noise ratio.

- The (expensive) tracking Compton camera performs quite better, with a much improved rejection of the activation backgrounds, even without making use of the direction information.

We found that we are not sensitive to the abundance of precious metals in the Pt family under these conditions.

Possible further developments of this work are the following:

- the exact angular dependence of gamma rays coming from the asteroid should be correctly simulated, in order to see the effect of possible background cuts based on their direction, especially with the Compton camera detectors;

- systematical effects should be completely taken into account: e.g. it could be useful varying the physics list used by the software;

- on the same topic, comparison with experimental results in literature could give a more detailed view on the problem.

A similar approach could be investigated for planetary surveys, with a portable camera, and applied to future missions, e.g. for the ground exploration on the planet Mars.

Acknowledgments

Bibliography

[1] P. A. J. Englert "Planetary gamma ray spectrometry: remote sensing of elemental abundances". In: *Proceedings in Radiochemistry A Supplement to Radiochimica Acta, vol. 1(1), 349-355.* (2011)

[2] A.A. Yaroshevsky et al. "The Mineral Composition of the Earth's Crust, Mantle, Meteorites, Moon, and Planets". In: *Advanced Mineralogy, Springer.* (1994)

[3] R. T. Dodd "Meteorites, a petrologic-chemical synthesis". *Cambridge University Press.* (1981)

[4] S. Li et al. "Water on the surface of the Moon as seen by the Moon Mineralogy Mapper: Distribution, abundance and origins". In: *Science Advances, vol.3(9).* (2017)

[5] "Apollo 15 Preliminary Science Report". *NASA Manned Spacecraft Center.* (1972)

[6] I. Adler et al. "Lunar Composition from Apollo Orbital Measurements". In: *IEEE Transactions on Nuclear Science, vol. 20(1), 24-32.* (1973)

[7] M. A. Van Dilla et al. "Lunar Composition by Scintillation Spectroscopy". In: *IRE Transactions on Nuclear Science, vol. 9(3), 405-412.* (1962)

[8] J. R. Arnold et al. "Gamma rays in space, Ranger 3". In: *Journal of Geophysical Research, vol. 67(12), 4878-4880.* (1962)

[9] A. E. Metzger et al. "Detection of an Interstellar Flux of Gamma-Rays". In: *Nature, vol. 204, 766-767.* (1964)

[10] A. P. Vinogradov et al. "Investigation of the intensity and spectral composition of the Moon's gamma-radiation at the Luna-10 automatic station". In: *Dokl. Akad. Nauk SSSR, vol. 170(3), 561-564.* (1966)

[11] W. C. Feldman et al. "The Lunar Prospector Gamma-Ray Spectrometer". In: *Lunar and Planetary Science, vol. 27, 355-356.* (1996)

[12] M. Kobayashi et al. "The Kaguya gamma-ray spectrometer: instrumentation and in-flight performances". In: *Journal of Instrumentation, vol. 8.* (2013)

[13] M. Naito et al. "Iron distribution of the Moon observed by the Kaguya gamma-ray spectrometer: Geological implications for the South Pole-Aitken basin, the Orientale basin, and the Tycho crater". In: *Icarus, vol. 310, 21-31.* (2018)

[14] J. Chang et al. "Gamma-Ray Detector on Board Lunar Mission Chang'e-1". In: *Journal of the Physical Society of Japan, vol. 78, 26-28.* (2009)

[15] M. Zhu et al. "Chang'E-1 Gamma-Ray Spectrometer and Its Preliminary Radioactive Results". In: *Planetary and Space Science, vol. 58, 1547-1554.* (2010)

[16] A. A. Siddiqi "Beyond Earth : a chronicle of deep space exploration, 1958-2016". By: *National Aeronautics and Space Administration, Office of Communications, NASA History Division.* (2018)

[17] I. Surkov et al. "Geochemical interpretation of the results of measuring gamma-radiation of Mars". In: *Proceedings of the Eleventh Lunar and Planetary Science Conference, vol. 1, 669-676.* (1980)

[18] J. I. Trombka et al. "Analysis of Phobos mission gamma ray spectra from Mars". In: *Proceedings of Lunar and Planetary Science Conference, vol. 22, 23-29.* (1992)

[19] W. V. Boynton et al. "Science Applications of the Mars Observer Gamma Ray Spectrometer". In: *Journal of Geophysical Research, vol. 97(5), 7681-7698.* (1992)

[20] W. V. Boynton et al. "Concentration of H, Si, Cl, K, Fe, and Th in the low- and mid-latitude regions of Mars". In: *Journal of Geophysical Research, vol. 112(E12).* (2007)

[21] J. O. Goldsten et al. "The MESSENGER Gamma-Ray and Neutron Spectrometer". In: *Space Science Reviews, vol. 131(1),339-391.* (2007)

[22] T. H. Prettyman et al. "Dawn's Gamma Ray and Neutron Detector". In: *Space Science Reviews, vol.163.* (2011)

[23] T. H. Prettyman et al. "Gamma-Ray and Neutron Spectrometer for the Dawn Mission to 1 Ceres and 4 Vesta". In: *IEEE Transaction on Nuclear Science , vol. 50(4), 1190-1197.* (2003)

[24] P. N. Peplowski et al. "Cosmogenic radionuclide production modeling with Geant4: Experimental benchmarking and application to nuclear spectroscopy of asteroid (16) Psyche". In: *Nuclear Instruments and Methods in Physics Research Section B, vol.446, 43-57.* (2019)

[25] P. N. Peplowski et al. "Gamma-Ray Spectroscopy of Asteroid 16 Psyche: Expected Performance of the Psyche Gamma-Ray Spectrometer". In: *47th Lunar and Planetary Science Conference, 1394.* (2016)

[26] L. Prockter et al. "The NEAR Shoemaker Mission to Asteroid 433 Eros". In: *Acta Astronautica, vol. 51(1-9), 491-500.* (2002)

[27] A. F. Cheng "NEAR Earth Asteroid Rendezvous: Mission Overview". In: *Space Science Reviews, vol. 82(1-2), 3-29.* (1997)

[28] J. O. Goldsten et al. "The X-Ray/Gamma-Ray Spectrometer on the Near Earth Asteroid Rendezvous Mission". In: *Space Science Reviews, vol. 82(1-2), 169-212.* (1997)

[29] J. I. Trombka et al. "Compostional mapping with the NEAR X-Ray/Gamma-Ray Spectrometer ". In: *Journal of Geophysical Research, vol. 102(E10), 23729-23750.* (1997)

[30] W. V. Boynton et al. "Elemental Composition of Asteroid 433 Eros: Results from the NEAR-Shoemaker X-Ray/Gamma-Ray Spectrometer and Comparison with Meteorites". In: *Meteoritics and Planetary Science Supplement, vol. 36, 27.* (2001)

[31] J. I. Trombka et al. "The NEAR-Shoemaker x-ray/gamma-ray spectrometer experiment: Overview and lessons learned". In: *Meteoritics and Planetary Science, vol. 36, 1605-1616.* (2001)

[32] J. S. Kargel "Metalliferous asteroids as potential sources of precious metals". In: *Journal of Geophysical Research, vol. 199(E10), 21129-21141.* (1994)

[33] E. Galimov et al. "Analytical results for the material of the Chelyabinsk meteorite". In: *Geochemistry International, vol. 51(7), 522-539.* (2013)

[34] E. Jarosewich "Chemical analyses of meteorites: A compilation of stony and iron meteorite analyses". In: *Meteoritics, vol. 25, 323-337.* (1990)

[35] M. L. Nelson et al. "Review of asteroid compositions.". In: *Resources of near-Earth space, 493 - 522.* (1993)

[36] S. Agostinelli et al. "GEANT4-a simulation toolkit". In: *Nuclear Instruments and Methods in Physics Research Section A, vol.506, 250-303.* (2003)

[37] A. C. Zoglauer et al. "MEGAlib: simulation and data analysis for low-to-medium-energy gamma-ray telescopes". In: *Proceedings of SPIE, vol.7011.* (2008)

[38] A. C. Zoglauer. "First Light for the Next Generation of Compton and Pair Telescopes". *PHD Thesis, Max Planck Institut für Extraterrestrische Physics.* (2005)

[39] A. C. Zoglauer et al. "Cosima - the Cosmic Simulator of MEGAlib". In: *IEEE Nuclear Science Symposium Conference Record 2009,2053-2059.* (2009)

[40] P. Jiggens et al. "The Solar Accumulated and Peak Proton and Heavy Ion Radiation Environment (SAPPHIRE) Model" In: *IEEE Transactions on Nuclear Science, vol. 65(2).* (2018)

[41] A. W. Strong et al. "Diffuse galactic emission measured by COMPTEL and the cosmic-ray electron spectrum". In: *The Astrophysical Journal Supplement series, vol.92, 425-428* (1994)

[42] A. De Angelis et al. "Introduction to Particle and Astroparticle Physics". *Springer International Publishing.* (2018)

[43] G. Lucchetta "Design and optimization around 1 MeV of a Tracker for a CubeSat Mission". *MasterThesis, University of Padova.* (2016)

[44] F. Berlato "Design and optimization around 1 MeV of a calorimeter for a CubeSat Mission". *MasterThesis, University of Padova.* (2016)

[45] R. Woolf et al. "Development of a CsI:Tl calorimeter subsystem for the All-Sky Medium-Energy Gamma-Ray Observatory (AMEGO)". In: *IEEE Nuclear Science Symposium and Medical Imaging Conference, proceedings paper.* (2019)

[46] G. Lucchetta et al. "Scientific Performance of a Nano-satellite MeV Telescope" In: *The Astronomical Journal, vol.153 (5).* (2017)

[47] L. G. Evans et al. "Preliminary Results of the NEAR Gamma-Ray Spectrometer". In: *Lunar Planetary Science, vol. 32.* (2001)

[48] L. G. Evans et al. "Elemental composition from gamma-ray spectroscopy of the NEAR-Shoemaker landing site on 433 Eros". In: *Meteoritics & Planetary Science, vol.36, 1639-1660* (2001)

[49] `https://www.spenvis.oma.be/help/background/gcr/gcr.html`

[50] `https://www.spenvis.oma.be/help/background/flare/flare.html`